(1)

Tunneling Acoustic Microscope

Keiji Takata

Advanced Research Laboratory, Hitachi Ltd.
Hatoyama, Saitama 350-03, Japan

July 1994

Abstract

This paper describes a new type of acoustic microscope based upon a scanning tunneling microscope (STM). This is an STM with an acoustic sensor that obtains physical information from an acoustic wave as well as the tunneling current. Interactions capable of generating strains in the STM sample are detectable and are used to image sample properties. This enhances STM's capabilities without reducing its ability, and enables imaging of nonconducting materials and imaging of dielectric and piezoelectric properties.

Contents

1. Introduction

The scanning tunneling microscope (STM)[1] has developed rapidly over the last ten years, due to its ability to directly image the geometric and electronic surface structures of conducting materials with atomic resolution. The STM is a new type of microscope that scans a probe tip over the sample surface mechanically, and thus no lenses or beams are required. The spacing between the tip and sample surface is controlled by detecting a tunneling current. Because the tunneling current rapidly decreases with increasing spacing,[2,3] the tunneling current flows only between the closest atoms on the tip and sample, which produces high horizontal, as well as vertical, resolution. By combining this tunneling effect with a three-dimensional piezoelectric actuator capable of positioning the tip on an atomic scale, an image of the sample surface can be obtained with atomic resolution. To achieve the ability, it is essential that the STM be rigid, in order to avoid changes in the tip-to-sample spacing due to external vibrations and furthermore to precisely control the tip position under the condition of surface forces. We can see the origin and the principle of STM in "topografiner".[4,5] The authors have already studied phenomena from field emission down to metal-vacuum-metal tunneling, as well as tip-position control using piezoelectric actuators.

The STM, however, can not be used to image nonconducting materials.

Meanwhile, the high positioning accuracy of piezoelectric actuators has also led to the development of other microscopes[6] which detect other kinds of interactions between the tip and the sample than the tunneling current. They use local probes based on, for example thermal conductivity (Scanning Thermal Profiler),[7] photon tunneling (Photon STM),[8] ion conductance (Scanning Ion-conductance Microscope),[9] electric capacitance (Scanning

Capacitance Microscope)[10] or the Hall effect (Scanning Hall Probe Microscope),[11] and obtain other information not derivable from electron tunneling. The spatial resolution greatly depends on the effective range of interaction. For long-range interactions, the spatial resolution depends on the geometrical shape of the tip, and so it is not easy to achieve high resolution stably. Among others, the atomic force microscope (AFM)[12] is one of the most successful, because it enables us to image nonconducting materials with atomic resolution, using forces between the tip, which is mounted on a microfabricated cantilever, and the sample. The forces are detected by optically monitoring the cantilever deflection caused by the forces. For sensitive force detection, the cantilever must be soft.

New microscopes should be created by combining ordinary techniques with two new concepts for STM: the piezoelectric actuators are capable of controlling the tip position on an atomic scale, and the spatial resolution depends on the effective range of interaction only. The excellent ability of STM is not reduced if only a sensor is added to the STM. For example, it is an interesting problem to add capability of observing both conducting and nonconducting samples to the STM.[13] This would enhance STM's ability to observe electronic states on an atomic scale, and enable us to observe, for example, electron interference patterns in a fine wire drawn on a nonconducting substrate. From this point of view, the AFM is capable, however, that is inherently not rigid due to the force detection system, which makes it difficult to use for the STM in which the tip-to-sample spacing must be precisely controlled in order to detect and control the tunneling current. The position of the tip on the soft cantilever is not controllable in three dimensions. As the spacing decreases, the attractive force becomes stronger and reaches a threshold where the force suddenly brings the tip into contact with the sample surface.[14] This also occurs as the tip is withdrawn from the surface. Thus, in the AFM, the spacing isn't necessarily controllable

over whole ranges of force. Besides, the lateral deflection of the cantilever induced by scanning, which causes distortion of images, also restricts control of the tip position.[15,16] The tip position is not known in three dimensions as accurately as the tip in the STM, which is connected rigidly to the piezoelectric actuators, because only the relative displacement of the rear surface of the cantilever is detected.

This paper describes a new type of STM-related microscope, called a tunneling acoustic microscope (TAM),[17-20] which combines techniques for generating and detecting acoustic waves with the STM, and is also a new type of acoustic microscope in line with the photoacoustic microscope (PAM),[21-23] electron acoustic microscope (EAM),[24,25] and scanning acoustic microscope (SAM).[26-28]

I turned to acoustics as the "ordinary technique", and started this work with the idea that since there are acoustic microscopes corresponding to the laser scanning optical microscope and the scanning electron microscope, it should also be possible to develop an acoustic microscope corresponding to the STM. If an interaction capable of generating a strain in the sample existed in the spacing like the thermal strains in the PAM/EAM, that interaction can be detected as an acoustic wave by adding an acoustic sensor to the STM. Fortunately, the STM has a special feature not found in the scanning photon/electron microscopes, that is, the mechanical scanning of the solid tip nearly contacting the sample surface, so that the TAM also has capability other than PAM/EAM. The capability is that the TAM can generate strains directly via the solid tip through forces between the tip and the sample, which makes it possible to observe both conducting and nonconducting materials with a rigid and simple system.

In Sec. 2, the principle and capability are presented, and the instrumentation is shown in Sec. 3. Section 4 describes and discusses the experimental results.

2. Principle

The principle of TAM is to detect a fine strain generated in a sample, thereby making it possible to obtain physical information on the source of the strain (Fig. 2.1). This detection is achieved through a device for detecting acoustic waves (usually utilizing a piezoelectric transducer) and through modulation of the interaction causing the strain. By the modulation, the strain, localized at the sample surface confronting the tip, is transmitted into the sample as an acoustic wave, and is detected by the piezoelectric transducer coupled to the sample. The amplitude of the generated acoustic wave corresponds to the modulation strength of the strain, and the phase of the wave also represents information on the interaction. Accordingly, interactions capable of generating a strain in sample are detectable.

We can consider atomic, electrostatic or magnetic forces as the interactions. Forces acting between the tip and the sample generate strains proportional both to the strength of the forces and to the elastic compliance of the sample, and either tip vibration or an ac voltage applied to the tip transforms the strain into an acoustic wave. Current injected into the sample from a STM tip should also induce thermal or electronic strains like those in PAM/EAM.[29,30] This is explained by the large current density (10^{10} A/m^2) due to the small injection area, although the absolute energy (10^{-9} W) is small in comparison with those of PAM/EAM.

The detected acoustic signals reflect the sample's elastic properties, to which the strains are intrinsically related. In experiments in the range of modulation frequencies of 10^8 – 10^9 Hz, reflection and diffraction of the acoustic wave occur and absorption also becomes significant. Just as in SAM, therefore, the detected signals should include acoustical information on the transmission process in the sample. And because the size of the source of

the ultrasonic wave generated in the sample surface is much less than the wavelength, the spatial resolution should be beyond the diffraction limit.

The spatial resolution with which both the interactions and the elastic properties are detected is not limited by the modulation frequency but by the extents of the strains, which are determined by the effective ranges of the interactions between the tip and the sample.

The only unique mechanical component of the TAM is the piezoelectric transducer, which does not reduce the capability or rigidity of the STM.

Surface forces, electrostatic forces, and piezoelectric strains have so far been detected and imaged. Not only the forces between the tip and the sample but also the properties of sample itself induce strains that are detected. In the experiments described here, however, the wavelength is on the order of the sample size so that neither reflection nor diffraction occurs. The generated acoustic wave therefore only transmits physical information on the interaction causing the strain and has no influence on spatial resolution and does not reflect the internal structure of the sample.

Magnetic forces and the current-induced strains have not yet been detected, but elastic properties have been imaged[31-33] and experiments with high-frequency modulation have been performed[34] by other researchers.

As described above, the TAM is analogous to the PAM/EAM and SAM, but there is a significant difference between the TAM and related techniques. The difference is caused by the fact that the STM involves scanning the sample mechanically, with the solid probe nearly contacting the surface. Using the tip, the TAM can therefore generate strains directly through forces between the tip and the sample, whereas the strains measured in the other techniques are mainly caused by heating the sample with beams of photons or electrons. The extent of cyclic thermal strain depends on not only the diameter of the beam but also the thermal

diffusion length μ_S determined by the modulation frequency f and by the thermal properties of the sample.[29] The basic relationship is $\mu_S \propto f^{-0.5}$. The thermal diffusion length is in the μm range at 1 MHz, but the thermal strain decreases with increasing modulation frequency. In the SAM using a focused ultrasonic beam as a probe, resolution is limited by the wavelength, which is on the order of sub-μm's. Meanwhile, both the extent and strength of the strains of TAM directly induced by the forces are independent of the modulation frequency but depend on the ranges of interactions and on the elastic properties of sample.

Tunneling acoustic microscopy thus offers spatial resolutions much higher than that of other acoustic microscopies. The repulsive region of the surface forces is a short-range interaction and we can therefore attain a high spatial resolution by using it as a feedback signal for controlling the tip-to-sample spacing. Electrostatic-force imaging, on the other hand, provides less spatial resolution but can be used to image sample's dielectric properties, etc. In detecting the piezoelectric effect, the spatial resolution depends on the thickness of the sample.

2. 1 Surface Force

The spacing between the tip and the sample is about one nanometer while tunneling, and at such a spacing forces act between them. Any force $\boldsymbol{F}$, for example an atomic force, acts between the nearest portions, generating strain S in the sample and also in the tip:

$$\boldsymbol{F}_{ij} = \boldsymbol{c}'_{ijkl} \cdot \boldsymbol{S}_{kl} ,$$

where $\mathbf{c}'$ is a value related to elastic constants of the sample. In air or between unclean surfaces, longer range forces act. Because the force strength varies with the spacing, tip vibration modulates the force so that the strain is also modulated, generating an acoustic wave corresponding to $\partial \boldsymbol{F}/\partial z$, where $\partial \boldsymbol{F}$ and ∂z are the force modulation and the tip vibration

amplitude, respectively. This acoustic wave is transmitted into the sample and is detected with the piezoelectric transducer coupled to the sample. The amplitude and the phase of the acoustic signal from the transducer represent the absolute value of the force gradient and the direction of the force, respectively. Thus we can measure the force by detecting the acoustic wave and can take the topography of nonconducting materials by keeping the amplitude constant instead of keeping the tunneling current constant. The measured surface contour is determined by the acoustic signal and thus essentially reflects elastic properties of sample. The influence of the elastic properties is not dominant, however, because the strength of the acoustic signal is strongly dependent on the tip-to-sample spacing. This is similar to the fact that differences in surface electric state induce few changes in tunneling gap and produce only less than sub-nm-height variation in the STM images.

2. 2 Electrostatic Force

Electrostatic force detection and some of its applications have already been demonstrated in atomic force microscopy.[35-37] In tunneling acoustic microscopy, the electrostatic force is detected as follows. When a voltage is applied between the tip and a conductive sample, the resultant electrostatic force corresponding to the voltage generates a strain in the sample. The strain is proportional to the force, and the proportional constant is the elastic compliance constant of the sample. By modulating the tip voltage, the strain is transmitted in the sample as an acoustic wave that can be detected. Accordingly, the electrostatic force is represented by the acoustic signal from the transducer. The amplitude corresponds to the force strength, but both polarities of the tip voltage yield the same phase signals because the electrostatic forces are always attractive if there is no fixed charge. The tip voltage $V\sin\omega t$ generates an

acoustic wave with a frequency of 2ω, where ω is angular velocity. When a tip voltage biased with a dc voltage of V ($V\sin\omega t+V$) is applied, the frequency of the generated wave corresponds to ω and the amplitude corresponds to a force strength of $2V$. For semiconductors, the force strength also depends on the polarity of tip voltages and represents the impurity concentration quantitatively. The electrostatic forces reflect dielectric and electric properties–such as capacitance between tip and sample, charge, electric potential, dielectric constant, impurity of semiconductor, and ferroelectric polarization. Accordingly, these properties are imaged. The electrostatic forces, however, interact over a long range, so they result in a spatial resolution, that is from hundred to several tens nm, considerably inferior to the resolution achieved with using the tunneling current or surface forces. This is a reason that the electrostatic forces are never used as a feedback signal to control the tip-to-sample spacing.

A quantitative estimation of the electrostatic forces acting on between a metal tip and a metal sample can be performed by concise calculations using the well-known method of images, as the tip-to-sample spacing is much larger than the radius of a hemispherical tip (Fig. 2.2). The electric field formed by the tip is nearly equivalent to the field formed by a point charge Q at the center of the tip sphere, and we can replace the force between the tip charge and the sample surface with the two charges interaction between the tip charge and another point charge placed symmetrically for the sample surface. The electrostatic force F is written as $F \propto V^2 \cdot r^2 / S^2$, where r, V, and S are the tip radius, applied voltage, and distance between the two charges, respectively. Thus, the detection of acoustic waves induced by the quantitatively estimated electrostatic forces reveals the force sensitivity of TAM.

2. 3 Piezoelectric Effect

Measuring the microscopic piezoelectric/electrostrictive (piezoelectric) effects by using the TAM enables us to image piezoelectric constants and polarization vectors and to obtain microscopic values for coercive electric fields with high spatial resolution.[38] This technique called Strain Imaging is microscopy to detect the strain generated in a piezoelectric film when a voltage is applied to the film by the tip. We can evaluate the characteristics of individual single crystals (each grain) in ceramics, when there is only one grain in the direction of thickness.

In tunneling acoustic microscopy, there are two methods for detecting strain. One is through detection of a vibration generated by applying an ac voltage from the tip to the piezoelectric film, using the piezoelectric transducer coupled to the back surface of the sample. The amplitude and phase of this vibration reflect the amplitude and direction of strain, respectively. The vibration brings the whole information throughout the strain-induced area. The extent of tip-voltage-applied area determines the lateral resolution. This area, however, is smaller than the tip radius ($\sim 10^2$ nm) because, since the dielectric constant of the film is large ($\sim 10^3$), the voltage applied to the piezoelectric film decreases rapidly with the increase of tip-to-sample spacing. Accordingly, the effectively vibrating area is, as described in Sec. 4, small enough to obtain good resolution.

The other method for detecting strain, which can be also used in the AFM or STM, is through detection of surface displacement caused by the strain, using a feedback loop to keep the tip-to-sample spacing constant. Because short-range surface forces are engaged in the feedback, the extent of strain-detected area is extremely small and does not limit the lateral resolution. We can measure the strain-versus-voltage curve for a small area (in other words, at a point), and this method can thus quantitatively measure the physical constants related to piezoelectric effect; that is, it can measure the piezoelectric constants and coercive electric

fields.

The detected strains depend on both characteristics of material itself and the angle between the polarization direction (*c*-axis) and applied electric field. The contribution of them can not be distinguishable. The piezoelectric constant ***d*** in bulk ceramics also consists of them, however, the contribution of angle distribution is averaged over all grains, so that the ***d*** constant is recognized as a value representing material characteristics. On the other hand, in this observation, the contributions of the angle distribution as well as material itself appear as strain variation of each grains.

When the polarization vector is normal to the sample surface (therefore parallel to the applied voltage) the amplitude and phase respectively correspond to the piezoelectric constant of the crystal without rotation of the polarization vector and the polarization direction if the applied voltage does not induce the reversals of the polarization vector. But generally we must take account of the angle between the polarization vector and the applied electric field, and both the polarization components in the direction of the applied electric field and the rotations/reversals of the polarization vector caused by the applied electric field contribute to the detected signals. The detection of this strain reveals physical information about piezoelectric effect, and when there is only one grain in the direction of thickness, we can evaluate the characteristics of individual single crystals (each grains) in ceramics.

3. Instrumentation

3. 1 Configuration

Figure 3.1 shows the major components of TAM. The piezoelectric transducer is coupled to the rear surface (or front surface) of the sample, and a lock-in amplifier (or similar electronics) is used to measure the output signal of the piezoelectric transducer. To generate the strains, the oscillator applies a sinusoidal voltage to either the z piezoelectric actuator or an electrochemically etched tungsten tip. The frequency of the sinusoidal voltage f is adjusted to the resonant frequency of the piezoelectric transducer, typically ~80 kHz. The x and y actuators have a sensitivity of 53 nm/V and that of the z actuator is either 53 or 27 nm/V, and the three actuators form a tripod. As shown in Fig. 3.1, the tip-to-sample spacing is controlled by a feedback loop using either the tunneling current or the acoustic signal generated by the repulsive surface force, since both are extremely sensitive to the spacing. The electrostatic force is not used for feedback control because it is a long-range interaction and its spatial resolution is therefore poor. The feedback loop using the acoustic signal uses a bandpass filter tuned to the oscillator frequency and an RMS/DC converter instead of a lock-in amplifier, and is as fast as that using the tunneling current. The servo electronics are used to control the z actuator so as to keep the feedback signal (surface force or tunneling current) equal to V_{ref}, and thus keep the spacing constant.

The scanning signals from the scanning electronics extend the x and y actuators in a raster manner to scan the tip over the sample. The z signals corresponding to the scanning signals form a topograph identified by either the surface force or the tunneling current. When the tunneling current is used as the feedback signal for conductive samples, the acoustic

signals from the piezoelectric transducer can be directly imaged corresponding to the scanning signals, and when the surface force is engaged in feedback control the tunneling current can be imaged simultaneously. To image other acoustic signals from the piezoelectric transducer, however, either of the two methods described below is used.

One is the time separation method,[39] which has been used in detecting electrostatic force. Other acoustic signals, for example, signals yielded by electrostatic forces, are detected momentarily at each pixel on a raster scan by the lock-in amplifier to which the output from the piezoelectric transducer is fed (Fig. 3.2). (1) After the scanning is locked at each pixel, the feedback operation is also locked and the tip position is kept constant. (2) The tip vibration is turned off and the other modulation is applied. In electrostatic force detection the spacing is extended to avoid current flow and prevent contact with the sample caused by the electrostatic force, and then an ac voltage is applied to the tip. After the amplitude and the phase of the induced acoustic wave are stored in the corresponding address of the frame memories, (3) the feedback operation and the scanning are resumed. This method allows us to measure the electrostatic force and the contours of the sample surface simultaneously.

Another method is the frequency separation method. To detect the other acoustic signals simultaneously, plural modulation frequencies, f' on top of f, are used (Fig. 3.3). The lock-in amplifier synchronized with the frequency f' is used in measuring other acoustic signals; for example, the vibration of the PZT. For sensitive detection, each of the frequencies f and f' is chosen to be equal to one of the resonant frequencies of the transducer. In the measurement, the tip voltage frequency f' and the tip vibration frequency f were fixed at the first and third resonant frequencies (typically ~70 kHz and ~210 kHz), respectively. Second resonant frequency was not generated, because bending mode of a circle transducer has been used and the vibration displacements therefore must be symmetrical

for the center axis. The coupling between the two frequencies is negligibly small in the experiments. The signal from the transducer is fed into the lock-in amplifier as well as into the bandpass filter tuned to f. The amplitude and phase signals from the lock-in amplifier that represent the piezoelectric properties of the sample are stored in the frame memories according to the scanning signals. The frequency separation method thus enables us to extract different kinds of information from the acoustic signals simultaneously.

While imaging the topography with surface force or tunneling current feedback, other information can be imaged simultaneously because the TAM has two eyes: the tunneling current and the acoustic signal.

3. 2 Ultrasonic Motor for Tip Approach System

In constructing an STM or one of the related microscopes, a tip approach system is the center of apparatus.[40,41] Because the piezoelectric actuators yield only μm-order extensions, a wide-range-positioning ability with high accuracy is required. The positioning range and the accuracy must be on the order of mm and sub-μm, respectively. Because only a little external vibration has a great influence upon the tip-to-sample spacing, the tip-to-sample mechanical loop must be rigid and small. And the tip approach system, that occupies the large part of the tip-to-sample mechanical loop, must also be rigid, compact, and remote controllable so that the whole system can be isolated from external vibrations. To achieve not only the vibration isolation but also thermal stability and fast scanning, the rigid and compact system is needed. Ultrasonic motors driven by friction forces are appropriate for such a system because they are simple, compact, rigid, and remote controllable.[42]

Figure 3.4 shows a new type of ultrasonic linear motor suitable for the tip approach system. Two rectangular piezoelectric plates ($25\times6\times1^t$ mm), Piezo 1 and Piezo 2, are

connected at both ends, and highly polished plates are bonded to the ends of Piezo 2. This motor moves on a flat stage. Piezo 1 is uniformly polarized in the thickness direction, but the two halves of Piezo 2 have opposite polarizations. Two sinusoidal voltages of the same frequency with a phase shift are applied to the top and bottom electrodes of Piezo 1 and Piezo 2. (1) The length vibration of Piezo 1 induces the bending vibration because the length of Piezo 2 is unchanged. The two vibrations compose the vibration shown in Fig. 3.5. (2) On the other hand, Piezo 2 generates a force, acting in the same direction on both ends, due to movement of the center of mass of Piezo 2, which produces a driving force in one direction. (3) By adjusting the phase between the vibrations induced by Piezo 1 and Piezo 2, elliptical vibrations are generated in both ends. The direction of the elliptical vibration can be controlled by the phase shift of the applied voltages. The resonant frequencies of length and bending vibrations due to Piezo 1 are respectively about 30 kHz and 56 kHz, and the resonant frequency due to Piezo 2 is about 62 kHz. Though the resonance frequencies are not the same, this motor operates correctly at the resonant frequency of length vibration of Piezo 1, ~56 kHz. The time required to move 50 mm is shown in Fig. 3.6 shows as a function of the phase shift between the applied sinusoidal voltages (20 $V_{p\text{-}p}$). Extremely small displacements are easily achieved with controlling the number of cycles in the applied voltage. Figure 3.7 shows the displacement as a function of the number of cycles, when the applied voltage is 25 $V_{p\text{-}p}$. A stable single step size down to 20 nm is allowable.

An ultrasonic motor made of piezoelectric plates measuring $13\times3\times1^t$ mm also moves correctly at 107 kHz. These motors can operate in an ultrahigh vacuum and at temperatures as low as 100 K. Their speed, however, depends on the contacting surfaces of the feet and stage, and the balance between the contacting forces at both ends also influences their operation.

A scanner is set on this ultrasonic motor, and the tip connected to the scanner approaches

the sample step by step. This motor is small and the tip and the scanner are held by frictional force so that the resonant frequency of the tip-to-sample mechanical loop becomes higher, allowing more flexibility in constructing the microscopes.

3. 3 Charge Control

The tip position is monitored by monitoring the voltages applied to the piezoelectric actuators of three-dimensional scanner, but the relations between the applied voltages and the extensions have large nonlinearity and hysteresis. Although the linearity and hysteresis of piezoelectric actuators can be greatly improved by controlling the applied charge instead of the voltage as described by C. V. Newcomb and I. Flinn,[43] their method is hardly used for quasi-static operation and I have therefore developed a new charge-control method suitable for STM.[44] A capacitor is connected to a piezoelectric actuator in series, so that the capacitor has the same quantity of charge as the actuator when a voltage is applied. This charge is proportional to the voltage applied to the capacitor, because the capacitance of capacitor C is always constant. Figure 3.8 shows the charge-control system, which consists of a feedback loop using the capacitor voltage equivalent to the charge. When an input signal V_{in} is fed into the circuit, the charge in the actuator Q is equal to $C \times V_{in}$. Figures 3.9 (a) and (b) show the extension as functions of voltage and charge, respectively. Both the linearity and hysteresis are extremely improved. Charge control is also achieved with integrating the current flowing into actuator, but this method is not stable because there is a time-dependent drift due to the bias current of the electronics. The residual hysteresis loop and the creep are inverse to those in voltage control, and this may be explained if we consider there were a few residual 90° domains having negative polarization for external electric field direction. Strain is proportional to the absolute value of polarization of domains for the external electric field

direction, but the charge condensed in the actuator also depends on the polarization direction. Accordingly, if 90°-rotation occurs from negative to positive polarization when a voltage is applied, a difference between the strain and the charge is produced and this difference causes the residual hysteresis and the creep.

4. Experimental Results and Discussion

4. 1 Surface Force Detection

Figure 4.1 shows the phase and amplitude of the acoustic signal output from the two-phase lock-in amplifier, as a function of the spacing.[17] The measurement was made in air while the tip was vibrated by applying a sinusoidal voltage (70 mV_{p-p}, 74.8 kHz) to the *z* actuator having a sensitivity of 53 nm/V. This frequency corresponded to the resonant frequency of the piezoelectric transducer. The sample was a conventionally cleaned silicon.

As the spacing decreased, the phase changed first one way and then the other, indicating a phase reversal. We must consider the changes in phase and amplitude on the basis of the noise as shown in Fig. 4.1. The noise was constant during the measurement. The change in phase clearly distinguishes between attractive and repulsive forces. When the force between the tip and the sample is attractive, the attraction is stronger the closer the tip gets, whereas when the force is repulsive, the opposite situation arises: hence the phase reversal between attractive and repulsive forces. After decreasing, the amplitude also increases as the spacing decreases. As shown in Fig. 4.1, when the two forces acting in the opposite directions add to the noise at the angles in sequence, the amplitude of the signal increases after decreasing. Accordingly, an attractive force acts on between the tip and the sample surface until the signal reaches its minimum; when the spacing becomes smaller, a strong repulsive force dominates the interaction between the tip and the sample. The effective range of the attractive force depends on the surface condition of the sample.

The advantages of TAM are its ability to detect surface forces continuously and to control the spacing over all ranges of forces: from strong repulsive forces to weak attractive forces.

This is essential for detecting tunneling current and forces simultaneously as described in Sec. 1. And because the repulsive force increases rapidly as the spacing decreases, this allows nonconducting materials to be observed with high resolution.

4. 2 Electrostatic Force Detection

The force detection in the TAM is sensitive enough to reveal details of surface forces and to enable the tunneling current to be controlled, but it is difficult to derive accurate quantitative figures from the output voltage of the piezoelectric transducer. Measuring the electrostatic force, however, permits quantitative estimation of the force sensitivity of TAM, because it is easy to calculate the strength of the electrostatic force quantitatively when the tip is hemispherical and the spacing is sufficiently larger than the tip radius, as described in Sec. 2.

Figure 4.2 shows measured (solid lines) and calculated (dotted lines) acoustic signals as a function of the tip-to-sample spacing.[19] The sample was Au deposited on Si connected to the ground. Sinusoidal voltages with amplitudes of +15 $V_{p\text{-}p}$ (0 – +15 V) and +20 $V_{p\text{-}p}$ (0 – +20 V) at frequency of about 80 kHz were applied to an electrochemically etched tungsten tip. It was confirmed with a scanning electron microscope (SEM) that the shape of the tip used in this experiment was hemispherical and that its apex radius was 60 nm. As shown in Fig. 4.2, the calculated force curves are in good agreement with the experimentally measured curves, allowing reliable quantitative estimation of the acoustic signals to be made. This proves that one division of oscilloscope scale, as you can see in the figure, corresponds to a force of 5×10^{-11} N and the noise amplitude is in lower level than the value. Accordingly, the TAM has a sensitivity of down to 10^{-11} N, which is two orders of magnitude smaller than an interatomic force.

4. 3 Surface Contour

Figure 4.3 shows the V-shaped groove topography of an optical disk made of UV resin without a conductive material coating.[17] The distance between the V-shaped grooves, as well as the depths of the grooves, was in good agreement with the designed values, proving the TAM to be reliable for imaging an insulating surface.

4. 4 Defects Induced by Thermal Oxidation

When a silicon wafer, which always contains superfluous oxide, is thermally oxidized the superfluous oxide precipitates in the wafer and forms defects. This is serious problem in semiconductor industry because the defects influence electric properties of semiconductor devices. The defects in silicon have so far been observed mainly by preferential etching, infrared tomography, or transmission electron microscopy,[45,46] but these techniques do not directly reveal electrical properties. The TAM, on the other hand, can sensitively image surface conductivity of a sample. We have been successful in observing the defects caused by the precipitation of superfluous oxide as changes in surface conductivity.[18]

The sample was prepared as follows. After conventional cleaning, a *p*-type silicon wafer (10 Ωcm) was thermally oxidized in steam at 1100 °C for two hours. A 0.2-μm-thick SiO_2 layer formed by the oxidation process was then removed by chemical etching using HF, and the sample was immediately loaded in the TAM in a vacuum ($\sim 10^{-7}$ Torr).

This sample is conductive enough to observe by using STM, but the topography was taken by using the feedback control of surface forces in order to detect the surface conductivity of sample itself. By fixing the tunneling spacing using surface force independent of the electric properties, the constant-force tunneling current imaging reflects the surface conductivity of sample itself. This is one of advantages of TAM. In the STM, on the

other hand, the whole conductance including both the tunneling spacing and the surface conductivity is kept constant, and changes in surface conductivity are therefore buried in topography as only slight changes in contour.

A electrochemically etched tungsten tip was vibrated by applying a sinusoidal voltage (~70 kHz, 20 mV_{p-p}) to the *z* actuator, and +1.6 V was applied to the tip. The detected tunneling current flowing between the tip and the sample was fed into the lock-in amplifier synchronized with the tip vibration frequency because the tunneling current was modulated by the tip vibration. The outputs from the lock-in amplifier were stored in the frame memories corresponding to the scanning signals, forming a constant-force tunneling current image.

The tunneling current image is shown in Fig. 4.4. This clearly shows low-resistance areas as white areas. The current was several tens of nanoamperes in the white areas but did not flow in the black areas. Low-resistance areas like those shown in Fig. 4.4 are never observed in samples that are not thermally oxidized as described above, and the low-resistance areas are equal in size to the pits observed in preferential etching. The white areas must therefore be formed by the defects due to the oxide precipitation during the thermal oxidation process.

A protrusion (Fig. 4.5) was observed only in the dashed-line area in Fig. 4.4, and in the other white areas the surface contour was flat on the order of one nanometer. The protrusion shown in Fig. 4.5 is about 5 nm high and its shape is good agreement with the current profile, although current did not flow in all regions of the protrusion. The two arrows in Fig. 4.5 correspond to the arrows in Fig. 4.4 and indicate the edges of the protrusion.

Using the current-constant feedback loop; that is, the STM; only flat or unrepeatable

images due to crush between the tip and the sample were taken and results corresponding to the images described above could not be taken. In scanning tunneling microscopy, changes in surface conductivity of a sample are translated into changes in the tip-to-sample spacing; thus changes in surface conductivity produce only little displacement of the tip because tunneling current is sensitive to the spacing. Furthermore, it is difficult to distinguish between tip displacements caused by changes in conductivity and those caused by surface contours. Protrusions as shown in Fig. 4.5 may cause the crush between the tip and the sample.

The constant-force tunneling current imaging of TAM makes it possible not only to observe the distribution of conductivity in a sample with both conducting and nonconducting regions, but also to observe changes in surface conductivity of the sample itself. In the TAM that detects both the forces and the tunneling current, the tip-to-sample spacing is fixed on the surface irrespective of the surface conductivity by the forces, and thus the detected tunneling current directly shows the conductivity of the sample surface itself including any nonconducting layer. The STM, on the other hand, hardly distinguish the surface conductivity of the sample itself from the tunneling conductance. Changes in surface conductivity are compensated for by changes in the spacing and appear only as slight changes in tip position. Moreover, it is difficult to distinguish such changes from topographic corrugations in the surface. Thus, the ability to maintain the tunneling spacing while imaging by the tunneling current is the most important difference between the TAM and the STM.

The changes in surface conductivity discussed in this section are not due to surface states on an atomic scale but are instead due to variations in the thickness of the surface silicon dioxide layer formed in air or to changes in resistance induced by fluctuation of impurity concentration. Changes in SiO_2 thickness, which cause changes in tunneling gap, greatly

appear in the tunneling current images, but it has so far been confirmed only that thermal-oxidation-induced defects cause changes in surface conductivity. Reaching more detailed conclusions will therefore require further studies.

4. 5 Ion-Implanted Silicon

This section presents sequential observations of ion-implanted silicon in order to determine the ranges both of the lateral spread of implanted ions and of the extent of lattice-damaged regions in silicon. These ranges are important for semiconductor devices, because they determine the channel length between the source and drain, which in turn determines device characteristics.

The sample was a *p*-type silicon wafer (ρ~10 Ωcm) implanted with As ($5\times10^{15}/cm^2$) at 80 keV through 18 nm of SiO_2 in a pattern of 1.5 μm lines and 1.2 μm spaces. The lattice-damage resulting from the ion-implantation transforms silicon single crystal into amorphous and creates nonconducting regions about 0.14 μm thick. Annealing removes the damage so that the regions become *n*-type.

First of all, the implanted sample from which the photoresist had been removed but which had not yet been annealed or etched was observed in air using the electrostatic force imaging and the surface force feedback.[19] This sample was, therefore, nonconducting over all regions, so we could not obtain information drawn from tunneling current.

Electrostatic forces are detected during the scanning stops at each pixel (256×256) of the image as follows (Fig. 3.2). By operating the apparatus shown in Fig. 4.6, the tip vibration is turned off and an ac voltage biased with a dc voltage ($V\sin\omega t + V$) is applied to the tip. Next, a dc voltage is applied to the *z* actuator while detecting the electrostatic forces. This increases

the spacing between the tip and sample in order to avoid current flow and contact caused by the electrostatic force. These procedures are performed almost simultaneously by a switch shown in Fig. 4.6. This method allows us to measure the electrostatic force and the contours of the sample surface simultaneously. In addition, the spacing makes it possible to apply a higher voltage to the tip, which improves sensitivity because the detected force increases with the square of the tip voltage.

Figure 4.7 shows the line profile image of topography, and Figures 4.8 show (a) the electrostatic force image and (b) the topography (measured simultaneously). Figures 4.9 are their line scan images. An ac voltage (+20 $V_{p\text{-}p}$ (0 – +20 V), ~80 kHz) was applied to the tip while an additional spacing of 0.7 nm was added to the tip-to-sample spacing. The electrostatic force image clearly distinguishes between the two regions by their different dielectric properties. Electrostatic force imaging should enable us to measure a lattice-damaged depth if we knew its dielectric constant. But because the difference between the electrostatic forces of different regions is caused not only by changes in both the thickness of the dielectric materials and their dielectric constants, the relation between the thickness and the dielectric constant of the lattice-damaged regions has not yet been determined. Tip-voltage-induced and fixed charges can be pointed out as the residual factors contributing to the measured forces. Furthermore, there must be contributions of surface-related charges, mainly absorbed H_2O, because this measurement was carried out in air. In order to achieve quantitative measurement of the lattice-damaged depth, it is necessary to distinguish between the contributions of these various influences. If the contributions such as fixed charges and absorbed H_2O are absent, the force ratio between negative and positive tip voltages quantitatively indicates the impurity concentration of semiconductor. The measured values, however, were not at all in agreement with the predicted values. For a metal sample the force

ratio is 1 and electrostatic forces are independent of the polarity of tip voltages. Because charges trapped in silicon dioxide layers or interfaces influence the characteristics of devices, further experiments using electrostatic force detection will reveal key features of microdevices: impurities, the thickness and dielectric constant of dielectric material on surface, fixed charges and absorbed molecules all contribute to electrostatic forces and consequently should be revealed by electrostatic force observation.

The topographs show that the implanted regions are about 15 nm lower than the other regions, which were covered with the photoresist and whose surface is an undamaged SiO_2 layer, and that their width is about 1.5 μm equal to the designed value. Considering the sputtering rate,[47] a large part of the height difference, 15 nm, results mainly from a sputtering effect, and allowing for volume expansion of the implanted regions, SiO_2 in the implanted region was either removed or mixed with the Si of the substrate. There are creases in the boundaries between the two regions. It becomes clear through this observation that these creases seen in regions covered with photoresist were formed by scattered atoms which were stopped by the photoresist and remained there. The creases are symmetrical, but in the electrostatic force image, that represents properties inside sample, they are asymmetrical, and a line can be seen on one side of the boundaries. This provides information on the interface between the surface nonconducting layer and the silicon substrate. This asymmetry also appears in the topography of samples after the removal of SiO_2 and after annealing, but its cause is not yet known. The other protrusions are residual photoresist, because the protrusions have the regularity of the photoresist pattern, and because they were never observed in the samples after etching to remove the silicon dioxide layer. Elastic properties of photoresist and silicon dioxide are fairly different, but because the topographic image was

the same with one taken with different surface forces the difference between elastic properties hardly contributes to the surface contours.

Owing to limited lateral resolutions caused by the long-range interaction of electrostatic force, a lateral spread of the lattice-damaged region can not be determined distinctly. The spread can, however, be discussed as follows. The slopes of forces in the boundaries in Fig. 4.9 (a) do not show a vertical profiling of the dopant but are instead mainly due to limited lateral resolution. This is because a cross-sectional image of a transmission electron microscope shows that the thickness of the lattice-damaged regions, ~0.14 μm, is uniform and the slopes shown in Fig. 4.9 (a) are not observed in the boundaries. As the tip-to-sample spacing is much smaller than the tip radius, only a limited area of the tip mainly interacts with its opposite area in the sample. When the tip is scanned across from a conductive region (or charge-trapped region) to a nonconducting region (or non-charge-trapped region), no large decrease in electrostatic forces occurs in the conductive region but begins to occur in the nonconducting region. Accordingly, the region showing uniformly strong forces and its surrounding region, from several tens up to one hundred nm, was not damaged, and a large part of the slopes are in the lattice-damaged regions. The lattice damage reached over the creases in the boundaries. And also considering the cause of the creases described above, it is reasonable to assume that the lateral spread of ions corresponds to the outside of the creases (Fig. 4.9).

Figures 4.10 and 4.11 show the pre-annealing topography and tunneling current image after etching, respectively.[17] The measurement was performed in a vacuum (~10^{-7} Torr) to avoid the native oxide growth. The samples were loaded into a vacuum chamber, after being slightly etched in a 0.05-N HF solution to remove the silicon dioxide layer. The etching

reveals conductive silicon surface without the lattice damage from the silicon dioxide layer. To avoid current flow caused by slight contact between the tip and sample, the tip was scanned slowly at 6.7 s/line. All topographic images were taken using the feedback loop of the acoustic signal. A sinusoidal voltage of 20 mV_{p-p}, at about 70 kHz, was applied to the *z* actuator having a sensitivity of 53 nm/V. The tip voltage was +6.9 V. The feedback loop adjusted the spacing to keep the current flow within a range from several to 100 nA in order to prevent damage to the tip or the sample As a result, the maintained force was repulsive.

The implanted regions were about 3 nm higher than the other regions, a relationship converse to that of the before-etching topography. It is clear that the original silicon surface is a surface in the regions completely covered with the photoresist because silicon single crystal is hardly etched by the HF solution, and accordingly, we must consider on the basis of the height of this surface. The 3-nm-height difference was caused by volume expansion due to the implantation that changed single-crystal silicon into amorphous. The value, 3 nm, is quantitatively good agreement with one calculated by the reason. The 3-nm-height corrugations we can see in the implanted region are roughness due to the implantation damage. The creases are also seen in the boundaries but the height variations there are smaller and asymmetrical. The asymmetry was predicted by the electrostatic force image capable of seeing inside properties of sample, and also taking account of appearance of asymmetry after removing the silicon dioxide layer, in conclusion, the forming of asymmetry occurred in the interface between the silicon dioxide layer and substrate. This asymmetry is not caused by the incident angle of implanted ion, because the topographs never show any asymmetry.

The tunneling current image, which clearly shows the conductive regions, proves that the

nonconducting region caused by the implantation-induced lattice damage extends outside the creases in the boundaries. This result is essentially drawn from the cause, that forms the creases, and is consistent with the creases being due to the cause discussed above. The extension of about 0.1 μm at both sides was induced by the lateral scattering of As within the substrate. The striped fluctuation of tunneling current shown in Fig. 4.11 is repeatable and consequently is not caused by changes in tip conductivity. It might show a microscopic part of the impurity-fluctuation-caused swirl that has been already presented in wafer scale observation.

Annealing for 10 min. at 1000 °C in nitrogen gas gets rid of the lattice damage and changes the implanted regions into *n*-type conductive silicon crystal, relaxing the volume expansion.[17] The regions are, however, about 4 nm lower (Fig. 4.12). This proves that not only SiO_2 but also Si atoms in the substrate were sputtered during implantation. The roughness seen in the before-annealing topography has been removed.

Figures 4.13 shows tunneling current images after annealing.[17] Current flow was from several to 100 nA. Arrows indicate creases in the boundaries. The tunneling current imaging shows that the nonconducting regions, including the whole areas of the creases, changed into *n*-type conductive regions. At the tip voltage of -1.9 V, the Fermi level of electrons in the tip is in the energy gap in *p*-type semiconductors, so that tunneling current does not flow. In Fig. 4.13 (a), the uniform black region where tunneling current was not detected corresponds to *p*-type region; the other regions are *n*-type. This result on the lateral spread is also consistent with prior results, since the creases were formed by the scattered atoms including As. I believe that the noise in the tunneling current image of Fig. 4.13 is mainly caused by variation of the thickness of residual SiO_2 on the surface. That is because tunneling current imaging is rather sensitive to changes in surface conductivity, and thus to differences in the

thickness of a nonconducting layer on the surface.

The conclusion drawn from the three experiments performed in sequence are as follows:

1) When As ions are implanted at 80 keV at a dose level of 5×10^{15} /cm^2, the range of lateral spread of the implanted ions is about 0.1 μm.

2) Under the condition of the implantation, both 18-nm-thick SiO_2 and 3-nm-thick silicon are sputtered and removed.

3) Scattered atoms form creases in the edges.

4) Further experiments are necessary to determine the cause of asymmetry between the creases that occurred in the interface between the SiO_2 and substrate or under the interface.

Figure 4.14 shows the schematic cross-section of the process.

4. 6 Contact Hole

This section describes observation of a contact hole in a 16-Mbit dynamic random access memory (DRAM).[20] To make topographic observations of semiconductor devices; for example, memory cells in DRAM, the SEM and recently the STM or AFM are generally used.[48] These observations have become more difficult, however, as packing density has been increased. In fact, the bottom of the contact hole in the 16-Mbit DRAM level is hardly visible with the commonly used SEM because of a remarkable decrease in the number of secondary electrons escaping from the hole. The STM can be used only for few devices because many semiconductor devices are nonconducting in part, and coating them with conductive material is not allowable for observing their fine structures.[49] In the AFM, lateral forces caused by steep slopes distort the images through an undesirable deflection of the cantilever.[16,50] And furthermore, for narrow and deep holes like the contact hole, the tip on

the cantilever is broken by the lateral deflection. One of the advantages of TAM, which allows good imaging of steep slopes to be obtained without any distortion caused by the lateral forces, is shown through the observation of memory cells with contact holes.

Observation of electric isolation or a connection between components in cells (bit line, word line, electrodes of transistors and capacitors, etc.) is also, of course, more important and difficult because such components are covered with a nonconducting layer. How components underlying a nonconducting layer are imaged by the electrostatic force measurement of TAM is also described in this section.

Figure 4.15 shows a schematic cross-sectional structure of a sample (16-Mbit DRAM) and shows the outline of the electrochemically etched tungsten tip used in this experiment. These contours are lines traced along those of the cross-section images obtained with the SEM. The tip is a commonly used one whose apex radius and diameter 2 μm from the tip apex are respectively ~0.07 μm and ~0.5 μm. The contact-hole is ~2 μm deep and ~0.3 μm in diameter at the bottom. The bottom surface can not be observed nondestructively with the SEM because most of the secondary electrons can not escape from the hole. Stacked capacitors covered with silicon dioxide ~0.6 μm thick are connected to a *p*-type silicon substrate (10 Ωcm, ground potential).

Figure 4.16 shows the topography of the sample. The tip traced the side walls of the narrow and deep holes precisely, reached the bottom of the holes, and scanned over the flat surface of the bottom. This shows that the feedback function of TAM controls the tip accurately, even for steep height variation. The diameters of the holes shown in Fig. 4.16, in contrast to those in an SEM image, appear smaller due to the finite size of the tip, and actually the difference between the diameters of the tip and the real contact-hole is equal to the

measured diameter in Fig. 4.16. This distortion of the image is inherent in the STM-type microscopes, but there is no difference between the slopes of the left and right sides in the hole and the image is consistent with one predicted from the SEM images shown in Fig. 4.15. Consequently, the TAM image is not distorted by lateral forces due to steep height variation.

Figures 4.17 show (a) an electrostatic force image and (b) a simultaneously taken topography. Here, an ac voltage, +40 $V_{p\text{-}p}$ (0 – +40 V) ~80 kHz, was applied to the tip, while an additional spacing of 0.7 nm was added to the tip-to-sample spacing. In Fig. 4.17 (a), the darker areas represent stronger forces. The strength of the electrostatic force mainly reflects the thickness of the silicon dioxide, so that the strongest forces were detected in the contact-holes. Outside the contact-holes, the electrostatic force image indicates the stacked capacitors embedded in the silicon dioxide, which is caused by a large contribution of the ground-connected stacked capacitors to the electrostatic force. The white areas around the holes are due to the absence of stacked capacitors as shown in Fig. 4.15, and the white lines between the holes show the spaces between the stacked capacitors. The dark areas like the one enclosed by the dashed line correspond to the stacked capacitors. Thus, the shapes of conductive components underlying the insulator are visible through electrostatic force.

In conclusion, the TAM is able to control a commonly used tip precisely along steep height variations with no influence of lateral forces. This enables us to nondestructively observe the contours of the bottom of deep and narrow holes at a high spatial resolution. Moreover, the conductivity of the bottom can be measured with the tunneling current. The topography is distorted because of the tip size, but the use of a whisker-like tip; for example, a semiconductor whisker with a diameter about 20 nm for several μm above the tip apex, will improve the distortion and permit observation in holes almost as narrow as the tip.

Electrostatic force images show electrically connected planes in a sense and so can be used to inspect the connection or isolation of components, including *pn* junctions, in stacked structures. A change in the polarity of the tip voltage yields a large difference in the electrostatic force for semiconductors, which should be used to quantitatively estimate the impurity concentration in semiconductors.

Thus, the abilities of TAM described in this section are significant from the viewpoint of inspection and development of semiconductor devices.

4. 7 Piezoelectric Thin Film

Lead-zirconate-titanate, PZT ($Pb(Zr_xTi_{1-x})O_3$), and its related perovskite materials are widely used for electromechanical transducers,[51,52] such as ultrasonic wave transducers or actuators. Recently, PZT has also attracted the attention of many researchers with other interests. Its large dielectric constants, for example, make it a suitable material for the dielectric layers of microcapacitors in semiconductor devices. It is also investigated for application in a nonvolatile memory using the switchable dielectric polarizations.[53-56] To use PZT in such microdevices, microscopic fluctuations of the characteristics will become a serious barrier, and a key technique will be making a PZT thin film having uniform characteristics on the order of nanometers. Accordingly, a high-resolution tool for observing the microscopic characteristics of the PZT thin films as-grown on an electrode (for example, Pt) is required.

Until now, ferroelectric materials have been observed by such means as optical microscopy, scanning or transmission electron microscopy and AFM.[57-59] Some of these techniques detect charges or stray electric fields of the surface, and some of them discriminate differences in lattice constants or use differences in etching rate. These method, however,

have poor resolution or they require etching or thinning of the sample.

The measurement using the TAM, that directly detects microscopic piezoelectric effects, enables us to image piezoelectric constants and polarization direction and to obtain microscopic values for coercive electric fields, all with high spatial resolution as described in Sec. 2. Figure 4.18 is a schematic diagram of the experiments. The sample is a 100-nm-thick layer of $Pb(Zr_{0.5}Ti_{0.5})O_3$ grown on a 100-nm-thick Pt layer by rf magnetron sputtering.[60,61] The Pt layer was formed on 400-nm-thick SiO_2 grown on a Si substrate by Ar sputtering. Observations using both an SEM and a transmission electron microscope have proven that the grain size is about 200 nm and there are only single grains in the direction of thickness. The piezoelectric transducer is coupled to the Si substrate, and the tip-to-sample spacing is feedback-controlled using tip vibration. A sinusoidal voltage of frequency f corresponding to one of the resonant frequencies of the transducer is applied to a piezoelectric plate (not shown in Fig. 4.18) to which the tip is coupled. Through surface force, the tip vibrated by the plate generates a vibration in the sample. The transducer detects the vibration and transforms it into an electric signal. After being amplified, the transducer signal is lock-in detected and the amplitude signal (that is, a feedback signal) is monitored by the servo electronics. The servo electronics, whose output is called the z signal, adjust the extension in the z direction of the scanner to keep the feedback signal constant. The z signals corresponding to scanning signals from the scanning electronics form a topograph.

To detect another vibration generated by the PZT, double modulation is used. Another lock-in amplifier synchronized with frequency f' of an ac voltage applied between the electrochemically etched tungsten tip and the Pt electrode is used in measuring strain signals of the PZT. For sensitively detecting the strain of the PZT through the output signal of the transducer, the tip voltage frequency f' is chosen to be equal to one of the resonant

frequencies of the transducer. This frequency f' and the tip vibration frequency f are fixed at the first and third resonant frequencies (typically ~70 kHz and ~210 kHz), respectively. The signal from the transducer is fed into the lock-in amplifier as well as into the servo electronics. The amplitude and phase signals from the lock-in amplifier are stored in the frame memories according to the scanning signals which represent the piezoelectric property of samples.

In detecting the strain by the feedback operation, f' is set to be much lower than the feedback response frequency, and the z signal, instead of the signal from the transducer, is fed into the lock-in amplifier. The z signals are also directly shown as a function of the tip voltage (applied electric field). This produces a curve of the induced strain versus the applied voltage, representing piezoelectric constants and coercive electric fields quantitatively. Another improvement of the imaging method in terms of scanning speed is that the modulation of feedback signals is detected by the lock-in amplifier when f' is adjusted to a frequency higher than the feedback response frequency.

Figure 4.19 shows the amplitude of vibrations generated by the tip voltage [+6 $V_{p\text{-}p}$ (0 – +6 V), 66.5 kHz] as a function of the tip-to-sample spacing. Such an alternating voltage biased with a dc voltage removes the influence of reversals of the polarizations from the detected signals. The sample in this measurement is a Sol-Gel processing $Pb(Zr_{0.52}Ti_{0.48})O_3$ film. The signal decreases rapidly with increasing spacing because the large dielectric constant results in the tip voltage being hardly applied to the PZT as the spacing becomes large. The vibration, however, was detected up to spacings of about 25 nm, and at such a spacing, the voltage applied in the PZT is only on the order of millivolts. The rapid decrease of the signal, which shows that the effectively vibrating area is narrow when the spacing is small, produces good lateral resolution, as described above. The dominant signals were detected through the spacing of 1.5 nm, so the extent of the effectively voltage-applied area,

that is, the tip area within the spacing of 1.5 nm, is a diameter of about 17 nm when the tip radius is 50 nm.

One example of the strains measured by the surface-displacement detection is shown in Fig. 4.20 as a function of the tip voltage. The curve shows butterfly-type hysteresis but has a strong asymmetry that should be caused by positive charges in the film.[62] The coercive voltages, -4.5 V and +2.5 V, are on the order of 10^7 V/m if the large part of the voltages were applied to the PZT film. The measured piezoelectric constants are on the order of 10^{-10} m/V. These values are consistent with the expected values.

Figures 4.21 (a) and (b) show amplitude and phase images of the strain, simultaneously taken by surface-displacement detection, respectively. The tip voltage, frequency, and scan area are -6 $V_{p\text{-}p}$, 133.3 Hz, and 10×10 μm. In the amplitude image, strain was detected in the bright portions whose outlines are formed by some circles, and the signal is almost at the level of noise in the dark portions. In the phase image it is noisy outside the circles because the signal was hardly detected. The crystallization of this sample was not good because of the bad Pb-composition, so the perovskite regions were circles and the rest of the film was amorphous.[61,62] The grains in the perovskite regions are not visible in the figures because the time constant of the lock-in amplifier (100 ms) is too large for this scanning speed (5 s/line).

Using vibration detection, we then observed the detailed structure in the perovskite regions. Figures 4.22 (a), (b), and (c) show simultaneously taken amplitude, phase and topographic images, respectively. The tip voltage, frequency, and scan area are +2 $V_{p\text{-}p}$, 78.6 kHz, and 8×8 μm. The curved surface in the topograph results from the bend of the scanner while scanning; the actual sample surface was flat. The maximum height variation in the topograph is about 10 nm, and most of the corrugations vary in height by several nanometers. Corrugations with a size of about 200 nm can be seen. The corrugations are equal in size to the grains of this film, and they therefore must represent the grains. The

center of the circle in this area is in the lower right part of the amplitude image, and arrows indicate several lines that extend like the spokes of a wheel. These lines are, of course, due to differences in piezoelectric property. Many grains having inverse polarization vectors are represented as visible white points in the phase image and as dark points in the amplitude image.

Thus, this method reveals the distribution of the region with piezoelectric effect and represents polarizations with lateral resolution on the scale of grain size. I believe that a single domain is formed grain by grain, since domains inside the grains were not observed.

The sensor in the TAM is the piezoelectric transducer, and by directly lock-in detecting the signals from the transducer we achieve a signal/noise ratio better than we get by *z*-signal detection. Vibration detection is therefore suitable for imaging. The sensitivity is down to ~0.1 Å. In the experiment, the frequency of the tip voltage was adjusted to the resonant frequency of the transducer for sensitive detection. In the subsequent steps, the detection of resonant frequencies in the direction of the thickness of piezoelectric film, by applying a tip voltage with a much higher frequency, is also important for revealing the elastic properties, thickness fluctuations, and electromechanical coupling coefficients of piezoelectric materials. In this case, the scannable spot source of ultrasonic waves will appear in the film, and reflection and diffraction will occur and also absorption will become significant in the sample as in scanning acoustic microscopy.[63)]

As to spatial resolution, surface-displacement detection is, in principle, superior to vibration detection because the area over which strain is detected is small and the extent of the area does not influence the spatial resolution, whereas in vibration detection the signal consists of vibrations of the whole area (down to 20 nm for a tip radius of 50 nm) to which the tip voltage is effectively applied. As shown in Fig. 4.22, however, we have obtained sufficiently good resolution to investigate material properties on a microscopic scale.

Although the induced strain essentially influences the lateral directions, this does not reduce the lateral resolution because the detected vertical strain is on the order of $10^{-10} - 10^{-11}$ m, and the lateral extent of the strain is also on the same order. It is difficult to discriminate differences in sample properties in the direction of thickness because the detected strains are signals integrated over all ranges of thicknesses This method is therefore not suitable for thick samples. It will result in the lateral resolution being determined by the thickness of the sample, and movement of the domain wall caused by the applied voltage.

The method described here measures the piezoelectric effect by applying voltages between the substrate electrode and a microelectrode (tip), and it yields information from the whole sample thickness. This microscopy is therefore suitable for characterizing materials for ultrasonic wave transducers because its operation is similar to this measurement. It is also suitable for characterizing materials for the dielectric layers of a capacitor because the piezoelectric effect is related to the dielectric property as well as the elastic property. This method makes it possible to measure reversals/rotations of polarization vectors microscopically, as shown in Fig. 4.20, which is useful for research on materials for memory using switchable dielectric polarizations. However it is necessary for precise quantitative evaluation to calibrate the net voltage applied to the piezoelectric film, because the tip voltage is also applied to the tip-to-sample spacing.

We can employ this method in the AFM if voltage is supplied to a conductive tip on the end of the cantilever so that cantilever deflection induced by the piezoelectric effect is detected. It should also be possible to use this method in the STM when a thin electrode is formed on the sample surface, in order to apply a voltage to piezoelectric materials. The STM can detect strain through the surface electrode, but in this case the lateral resolution would be reduced by the surface electrode, and also, the distribution of polarizations might change because the electric potential of the surface is uniform.

5. Conclusion

The TAM is an STM with an acoustic sensor, and obtains physical information from acoustic waves as well as from the tunneling current. The TAM enhances the capability of STM so that we can observe both nonconducting and conducting materials using both forces and tunneling current. A sensitive and rigid force detection system makes it possible to control the tip position continuously over all ranges of forces. The simultaneous detection of forces and tunneling current permits the electronic properties of the sample itself to be observed independently of the tunneling conductance. Electrostatic force detection proves that TAM has a sensitivity of down to 10^{-11} N, and is used to show the dielectric characteristics of a sample. Strain imaging enables us to reveal microscopic piezoelectric properties.

I have discussed the primary capabilities of TAM, but there are others yet to be achieved, as described in Sec. 2. Adding other ultrasonic techniques should further increase the range of applications for this microscopy.

Acknowledgements

I wish to thank Dr. Hiromichi Shimizu for providing the trigger for this work and for his valuable advice, Dr. Takehiro Okawa, Mr. Koichi Ono and Dr. Masao Hotta for his technical support on the electronics, Dr. Masatada Horiuchi, Dr. Nobuyoshi Natsuaki, Dr. Takashi Takahama, Dr. Keizo Kato, Dr. Jiro Yugami, Dr. Shigeru Jomura, Dr. Keiko Kushida, Dr. Kazuyoshi Torii, Dr. Hiroshi Miki and Dr. Tokuo Kure for preparing the samples and discussion, Mr. Shingo Nakagawa for observing many tips with the SEM, Dr. Tohru Ishitani, Dr. Atsushi Hiraiwa, Mr. Yoshimi Kawanami and Mr. Yuichi Madokoro for their valuable discussions on ion implantation, and Dr. Tatsumi Mizutani, Dr. Yasuhiro Mitsui and Dr. Katsumi Miyauchi for their helpful discussion throughout my work.

References

1) C. Binning, H. Rohrer, Ch. Gerber, and E. Weibel: Phys. Rev. Lett. **49** (1982) 57.

2) J. G. Simmons: J. Appl. Phys. **34** (1963) 1793.

3) E. L. Wolf: *"Principles of Electron Tunneling Spectroscopy"*, (Oxford science publications, 1985).

4) R. Young, J. Ward, and F. Scire: Rev. Sci. Instrum. **43** (1972) 999.

5) R. Young, J. Ward, and F. Scire: Phys. Rev. Lett. **27** (1971) 922.

6) H. Rohrer: Ultramicroscopy **42-44** (1992) 1.

7) C. C. Williams, and H. K. Wickramasinghe: Appl. Phys. Lett. **49** (1986) 1587.

8) R. C. Reddick, R. J. Warmack, D. W. Chilcott, S. L. Sharp, and T. L. Ferrell: Rev. Sci. Instrum. **61** (1990) 3669.

9) P. K. Hansma, B. Drake, O. Marti, S. A. C. Gould, and C. B. Prater: Science **243** (1989) 641.

10) C. C. Williams, W. P. Hough, and S. A. Rishton: Appl. Phys. Lett. **55** (1989) 203.

11) A. M. Chang, H. D. Hallen, L. Harriott, H. F. Hess, H. L. Kao, J. Kwo, R. E. Miller, R. Wolfe, and J. van der Ziel: Appl. Phys. Lett. **61** (1992) 1974.

12) C. Binning, and C. F. Quate: Phys. Rev. Lett. **56** (1986) 930.

13) S. Morita, T. Ishizawa, Y. Sugawara, T. Okada, S. Mishima, S. Imai, and N. Mikoshiba: Jpn. J. Appl. Phys. **28** (1989) L1634.

14) T. P. Weihs, Z. Nawaz, S. P. Jarvis, and J. B. Pethica: Appl. Phys. Lett. **59** (1991) 3536.

15) S. Akamine, R. C. Barrett, and C. F. Quate: Appl. Phys. Lett. **57** (1990) 316.

16) A. J. den Boef: Rev. Sci. Instrum. **62** (1991) 88.

17) K. Takata, T. Hasegawa, S. Hosaka, S. Hosoki, and T. Komoda: Appl. Phys. Lett. **55** (1989) 1718.

18) K. Takata, J. Yugami, T. Hasegawa, S. Hosaka, S. Hosoki, and T. Komoda: Jpn. J. Appl. Phys. **28** (1989) L2279.

19) K. Takata, T. Okawa, and M. Horiuchi: Jpn. J. Appl. Phys. **30** (1991) L309.

20) K. Takata, T. Kure, and T. Okawa: Appl. Phys. Lett. **60** (1992) 515.

21) A. Rosencwaig, and A. Gersho: J. Appl. Phys. **47** (1976) 64.

22) R. J. von Gutfeld, and R. L. Melcher: Appl. Phys. Lett. **30** (1977) 257.

23) A. Rosencwaig, and G. Busse: Appl. Phys. Lett. **36** (1980) 725.

24) E. Brandis, and A. Rosencwaig: Appl. Phys. Lett. **37** (1980) 98.

25) C. S. Cargill III: Nature **286** (1980) 691.

26) R. A. Lemons, and C. F. Quate: *Proc. 1973 IEEE Ultrasonics Symp.* (1973) 18.

27) B. Hadimioglu, and C. F. Quate: Appl. Phys. Lett. **43** (1983) 1006.

28) A. Briggs: *"An Introduction to Scanning Acoustic Microscopy"*, (Oxford University Press, New York, 1985).

29) *"Photoacoustic and Photothermal Phenomena III"*, ed. Bicanic **69** (Springer-verlag, New York, 1991) .

30) R. G. Stearns, and G. S. Kino: Appl.Phys.Lett. **47** (1985) 1048.

31) P. Gleyzes, P. K. Puo, and A. C. Boccara: Appl.Phys.Lett. **58** (1991) 2989.

32) O. Kolosov, and K. Yamanaka: Jpn. J. Appl.Phys. **58** (1991) 1103.

33) B. Cretin, and F. Stahl: Appl.Phys.Lett. **62** (1993) 829.

34) S. Akamine, B. Hadimioglu, B. T. Khuri-Yakub, H. Yamada, and C. F. Quate: *Proc. 1991 IEEE Ultrasonics Symp.* (1991) 857.

35) Yves Martin, David W. Abraham, and H. Kumar Wicramasinghe: Appl.Phys.Lett. **52** (1988) 1103.

36) J.E.Stern, B. D. Terris, H. J. Mamin, and D. Rugar: Appl.Phys.Lett. **53** (1988) 2717.

37) B. D. Terris, J.E.Stern, D. Rugar, and H. J. Mamin: Phys.Rev.Lett. **63** (1989) 2669.

38) K. Takata, K. Kushida, K. Torii, and H. Miki: Jpn. J. Appl. Phys. **33**, No.5B (1994).

39) R. J. Hamers, R. M. Tromp, and J. E. Demuth: Phys. Rev. Lett. **56** (1986) 1972.

40) K. Takata, S. Hosoki, S. Hosaka, and T. Tajima: Rev. Sci. Instrum. **60** (1989) 789.

41) Y. Kuk, and P. J. Silverman: Rev. Sci. Instrum. **60** (1989) 165.

42) K. Takata: *Proceedings of 12th Symposium on Ultrasonic Electronics, Tokyo 1991,* Jpn. J. Appl. Phys. 31 (1992) Suppl. 31-1, 3.

43) C. V. Newcomb, and I. Flinn: Electron. Lett. **18** (1982) 442.

44) K. Takata et al.: *Extended Abstracts of the 34th Spring Meeting of the Japan Society of Appl. Phys. and related societies, Tokyo, March,* 28p-L-1 (1987).

45) S. Sadamitsu, S. Sumita, N. Fujino, and T. Shiraiwa:
Jpn. J. Appl. Phys. **27** (1988) L1819.

46) K. Yamabe, and K. Taniguchi: IEEE J. Solid-State Circuit SC-**20** (1989) 343.

47) G. Betz, and G. K. Wehner: "*Sputtering by Particle Bombardment I*", ed. R. Behrisch (Springer-verlag, New York, 1981) 58.

48) K. Saito, M. Yoshizawa, and K. Wada: J. Vac. Sci. Technol. **B8** (1990) 1152.

49) I. Tanaka, F. Osaka, T. Kato, Y. Katayama, S. Muramatsu, and T. Shimada:
Appl. Phys. Lett. **54** (1989) 427.

50) S. Akamine, R. C. Barrett, and C. F. Quate: Appl. Phys. Lett. **57** (1990) 316.

51) M. M. Farrow et al.: Applied Optics **17** (1978) 1093.

52) N. Mikoshiba et al.: *Proc. 1980 IEEE Ultrasonics Sympss.* (1980).

53) C. Araujo, J. Scott, R. Godfrey, and L. McMllan: Appl. Phys. Lett. **48** (1986) 1439.

54) W. Kinney, W. Shepherd, W. Miller, J. Evans, and R. Womack:
Tech. Dig. IEDM 87 (IEEE New York, 1986) 850.

55) S. Eaton, D. Butler, M. Paris, D. Wilson, and H. McNeile:
Tech. Dig. ISSCC 88 (1988) 130.

56) J. Evans, and R. Womack: IEEE J. Solid State Circuits **23** (1988) 1171.

57) M. Tanaka, and G. Honjo: Jpn. J. Appl. Phys. **19** (1964) 954.

58) L. A. Bursill, Peng Ju Lin, and Feng Duan: Philos. Mag. A **48** (1983) 953.

59) F. Saurenbach, and B. D. Terris: Appl. Phys. Lett. **56** (1990) 1703.

60) K. Torii, T. Kaga, K. Kushida, H. Takeuchi, and E. Takeda:
Jpn. J. Appl. Phys. **30** (1991) 3562.

61) to be published.

62) K. Carl, and K. Härdtl: Ferroelectrics **17** (1978) 473.

63) C. F. Quate, A. Atalar, and H. K. Wickramasinghe: *Proc. IEEE* **67** (1979) 1092.

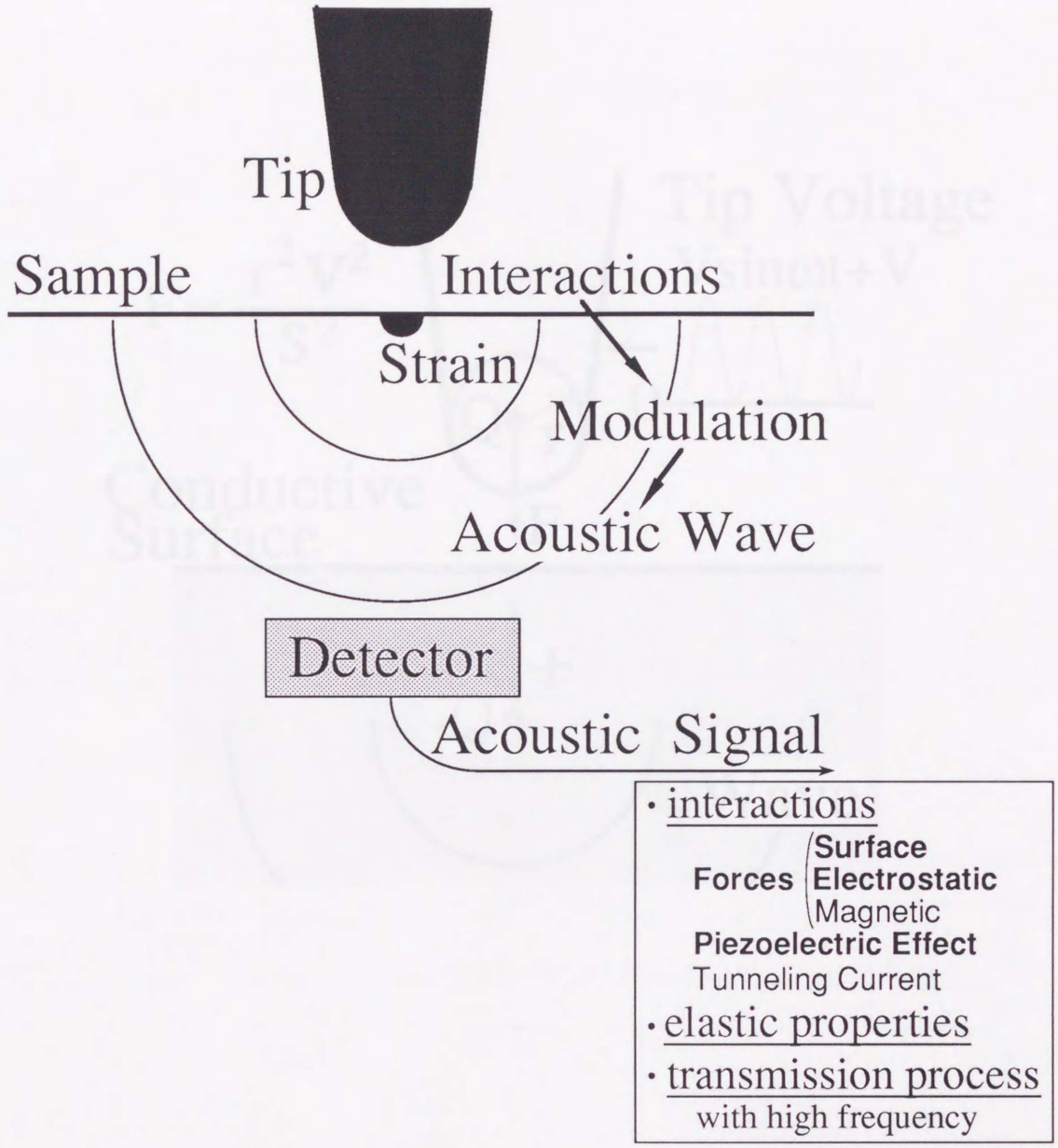

Fig. 2.1. Principle of tunneling acoustic microscopy.

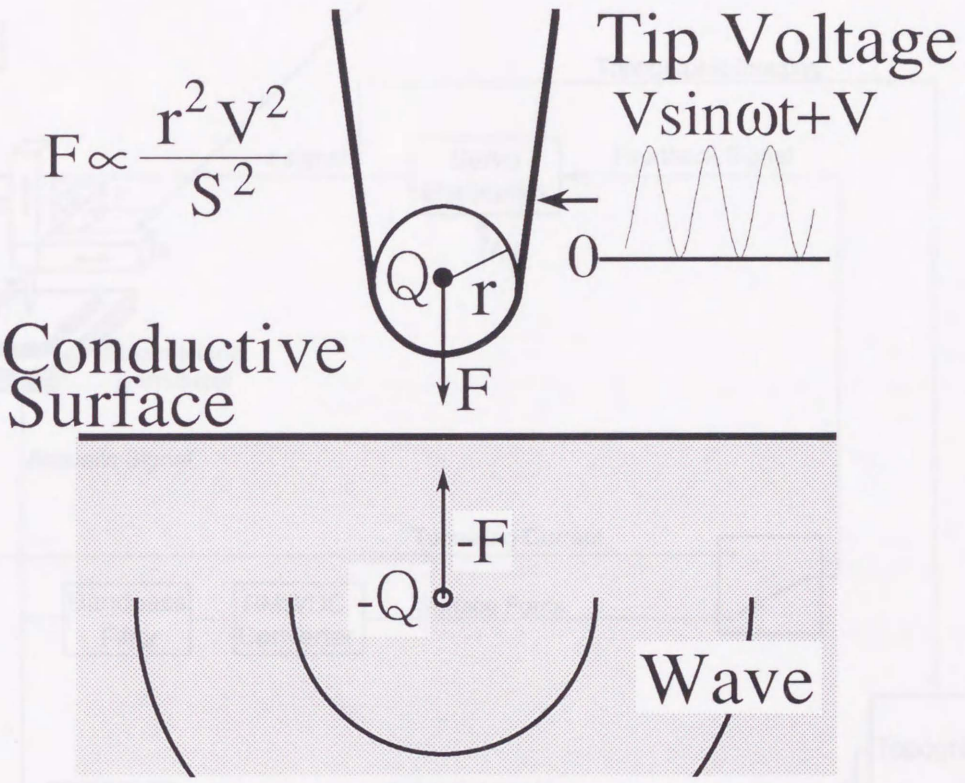

Fig. 2.2. Principle of electrostatic force detection.

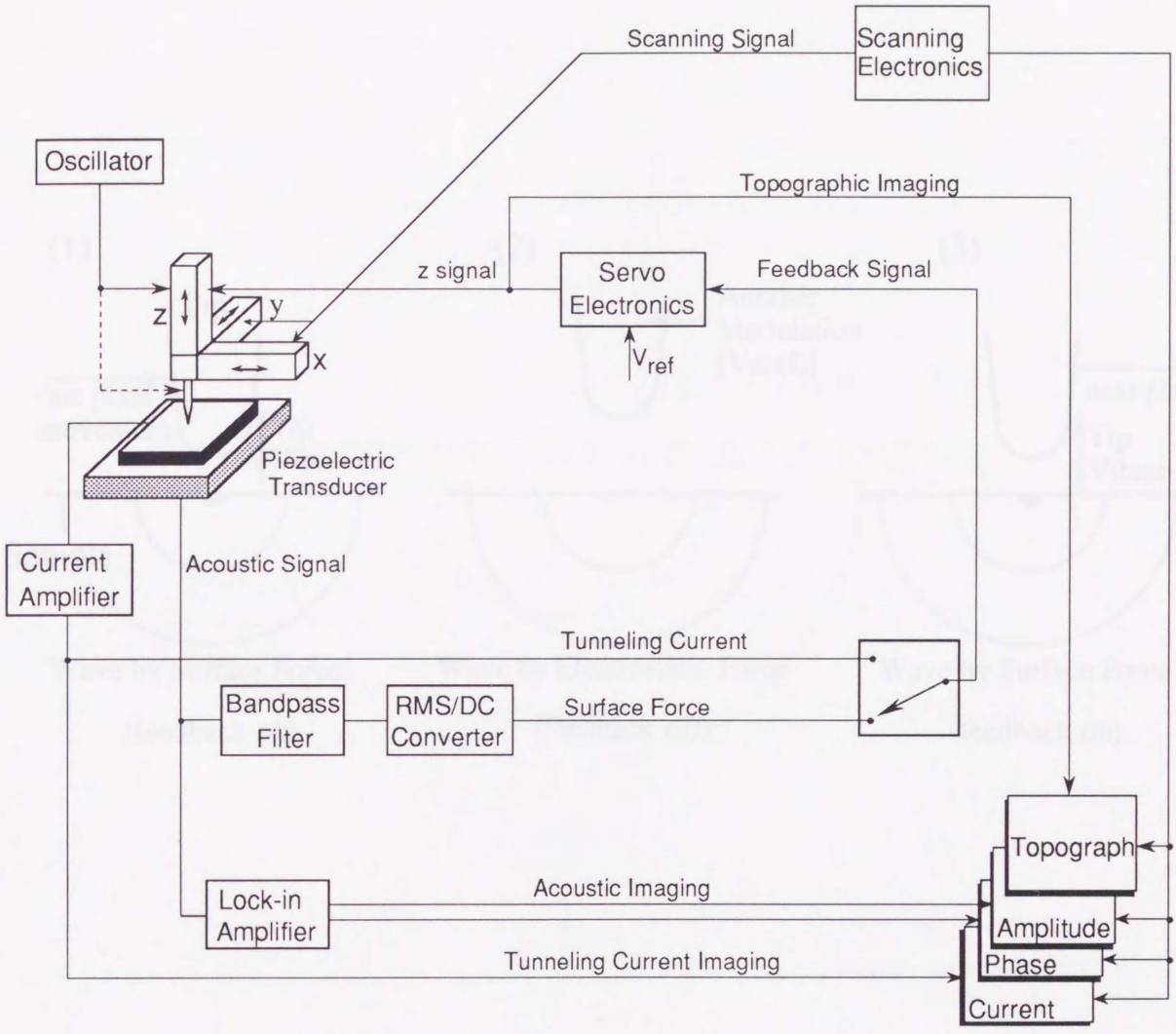

Fig. 3.1. Schematic diagram of a tunneling acoustic microscope.

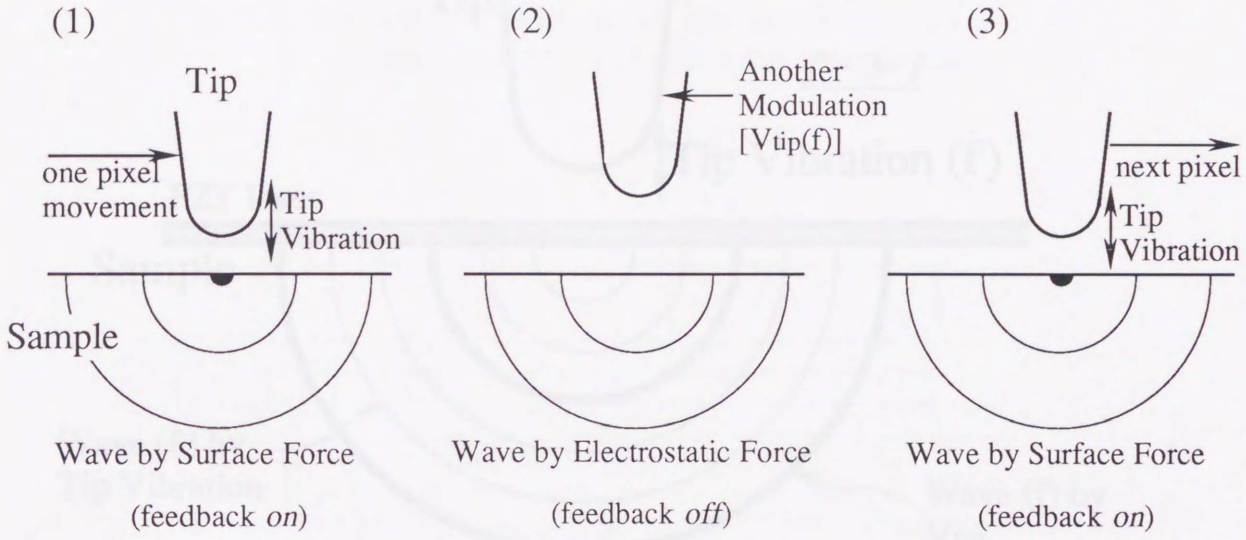

Fig. 3.2. Sequence of time separation method.

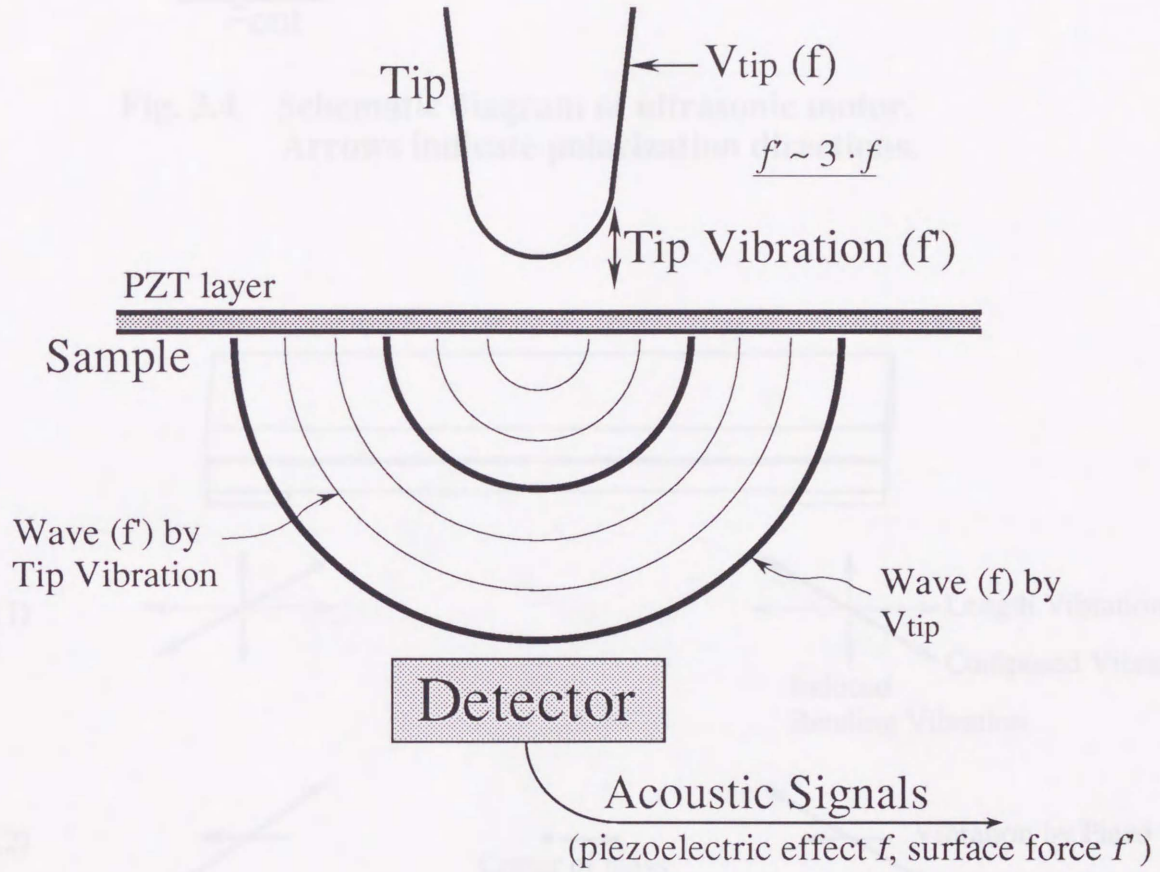

Fig. 3.3. Schematic diagram of frequency separetion method.

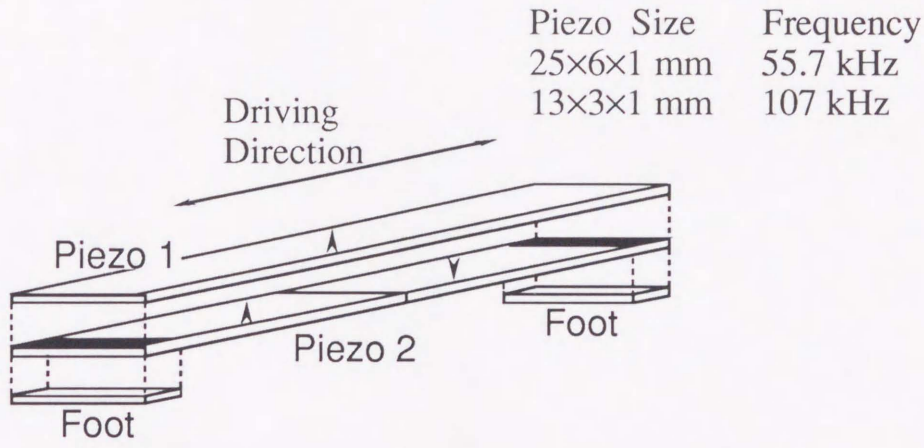

Fig. 3.4. Schematic diagram of ultrasonic motor. Arrows indicate polarization directions.

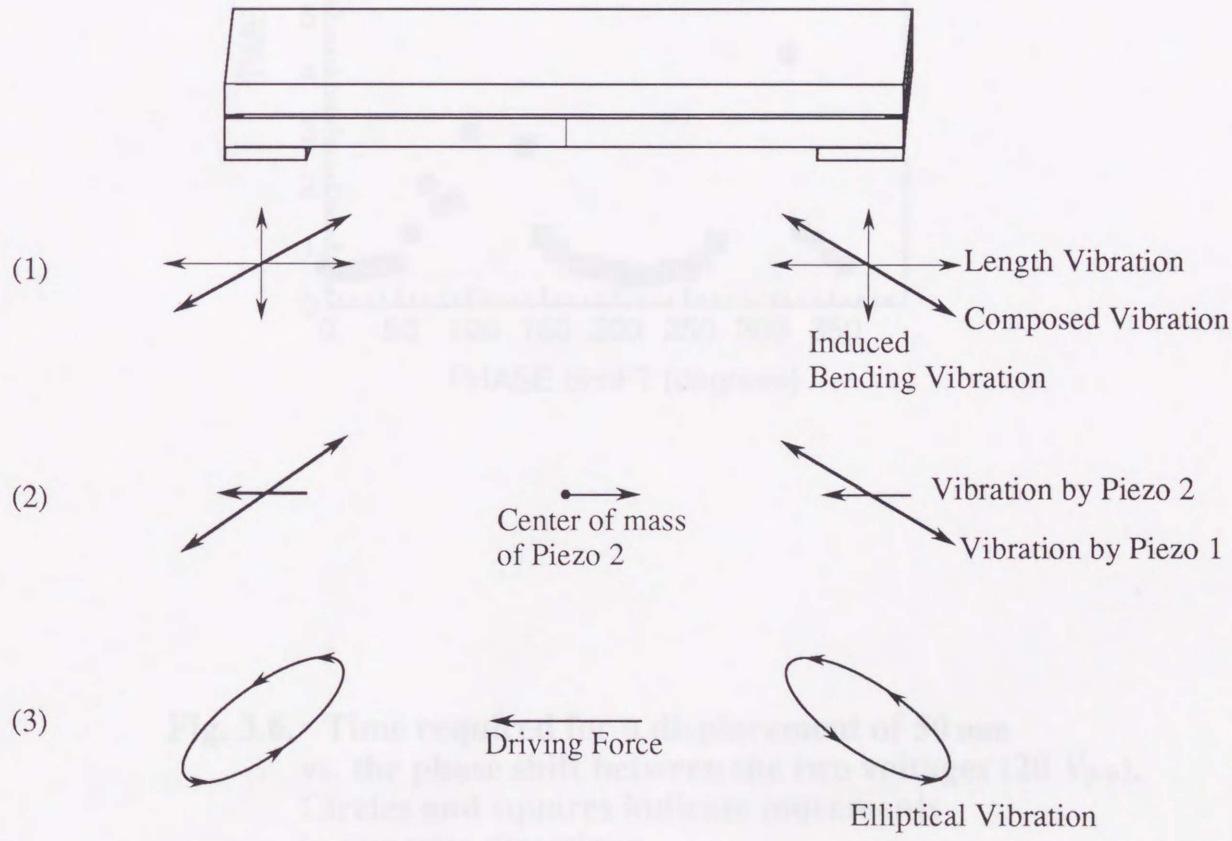

Fig. 3.5. Scheme of vibration displacements of feet.

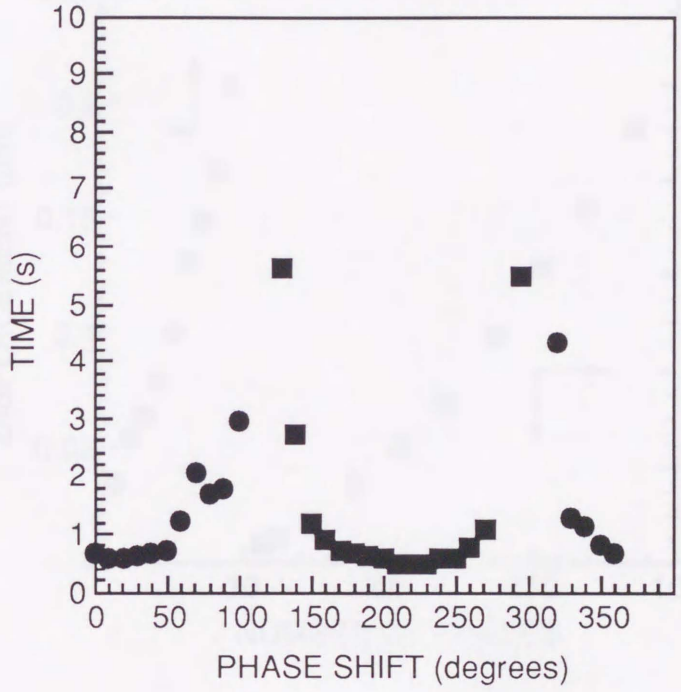

Fig. 3.6. Time required for a displacement of 50 mm vs. the phase shift between the two voltages (20 V_{p-p}). Circles and squares indicate movements in opposite directions.

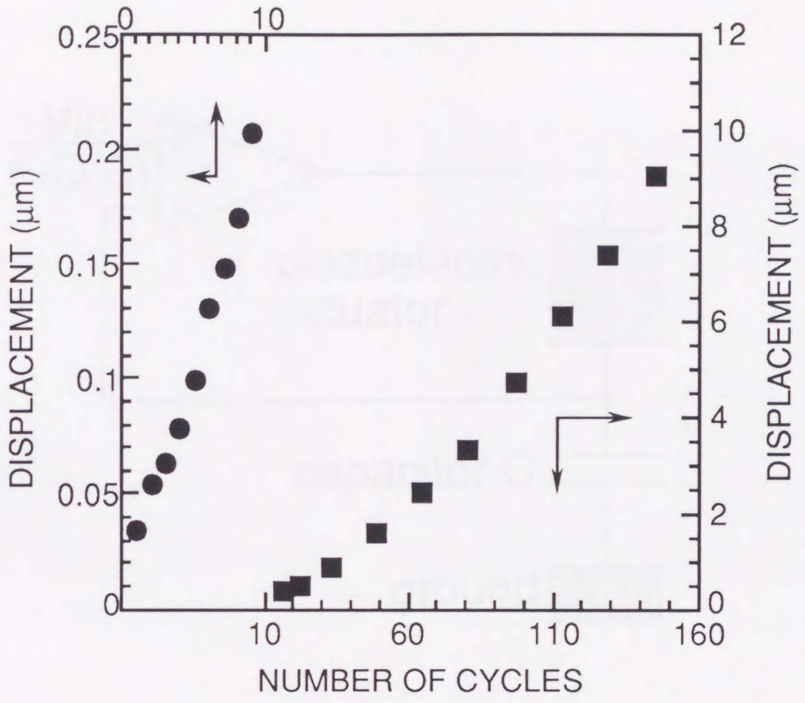

Fig. 3.7. Displacements as a function of number of cycles (25 V_{p-p}).

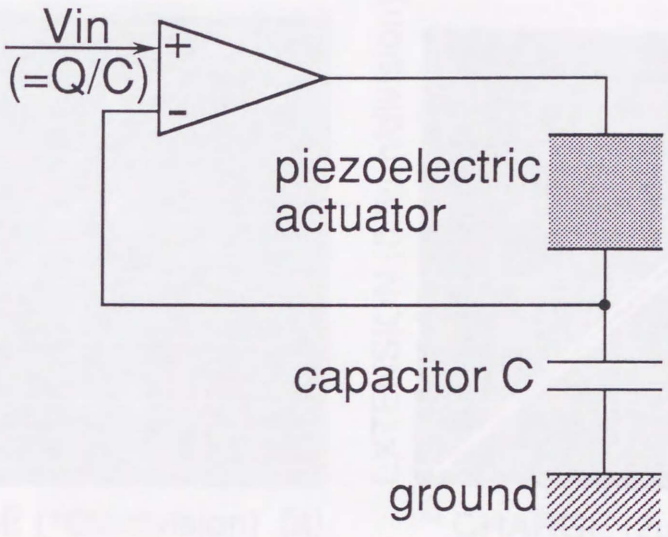

Fig. 3.8. Diagram of charge-control system.

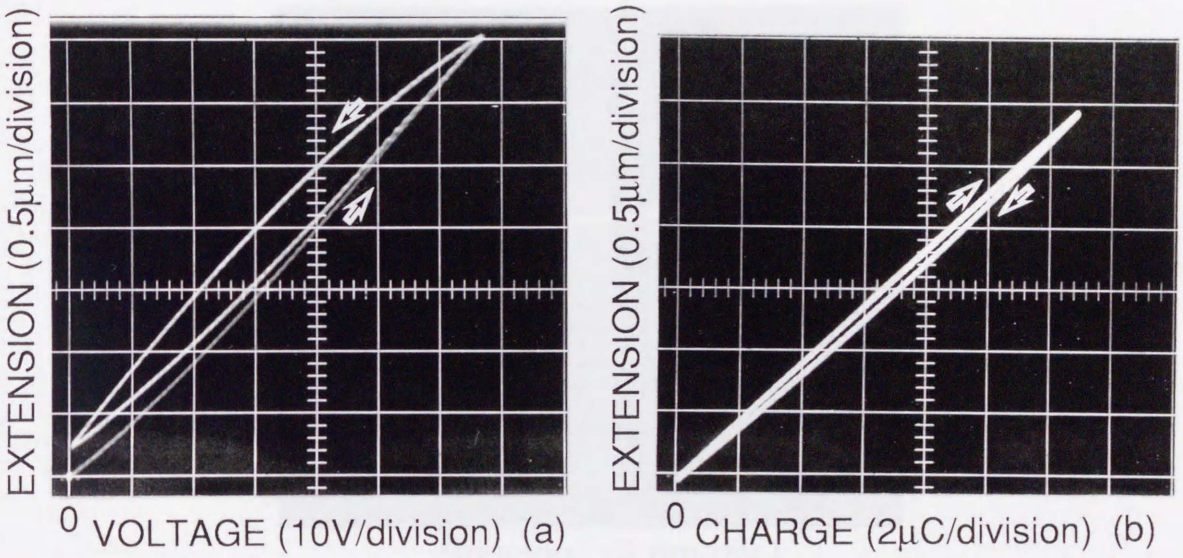

Fig. 3.9. Extension as a function of (a) voltage and (b) charge.

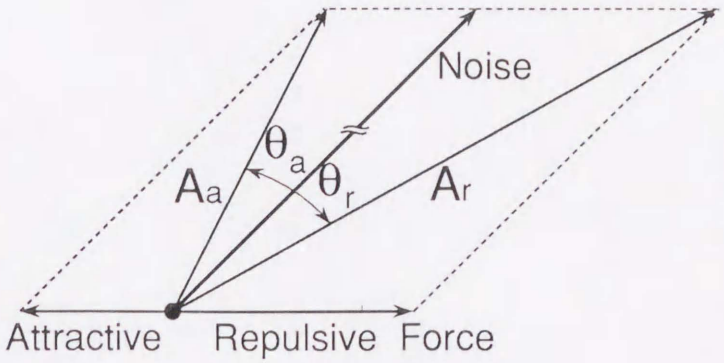

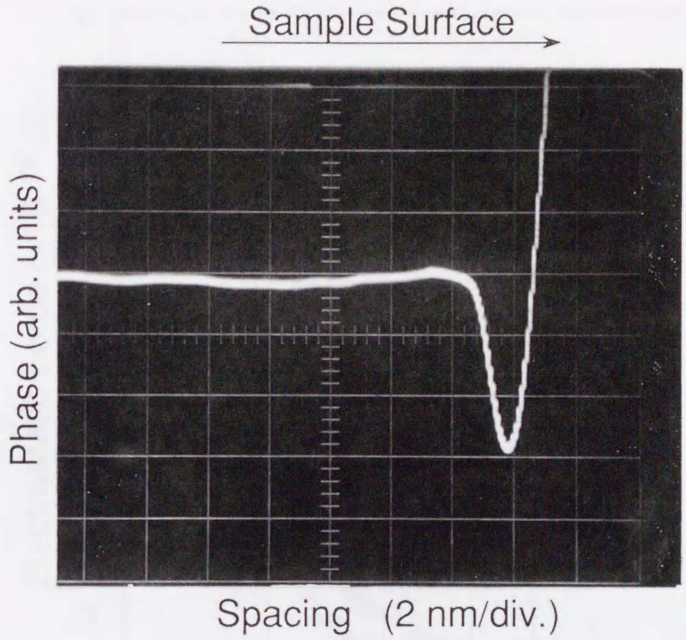

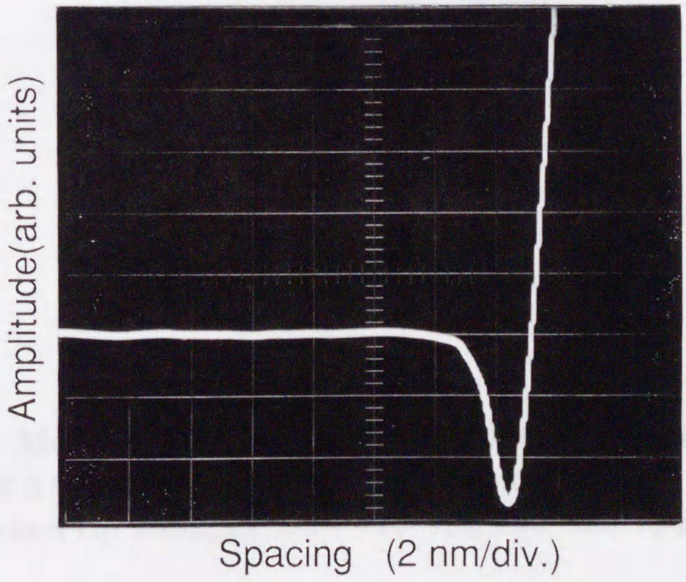

Fig. 4.1. Acoustic signals as a function of spacing.

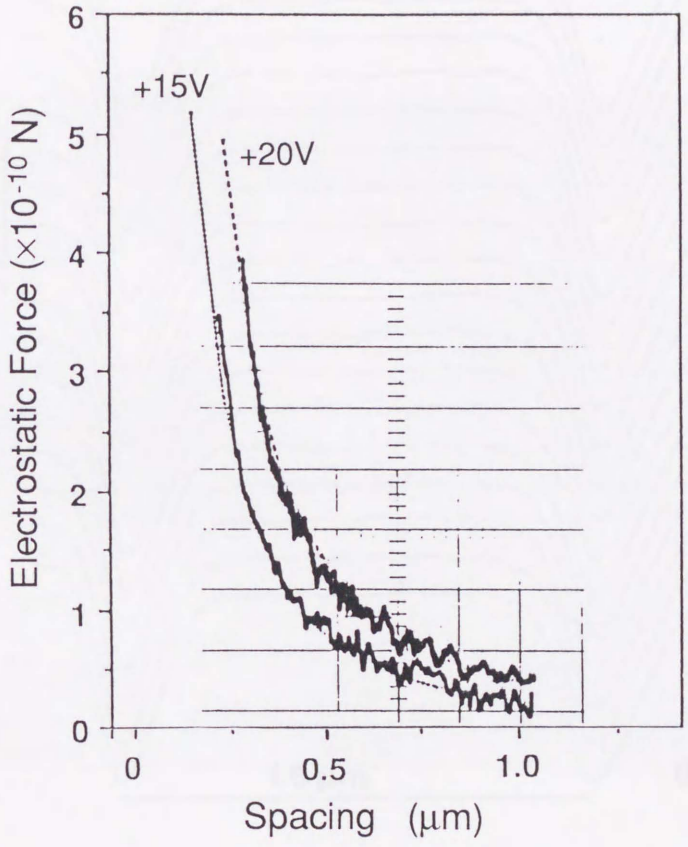

Fig. 4.2. Measured (solid lines) and calculated (dotted lines) forces as a function of tip-to-sample spacing when tip voltages were +15 $V_{p\text{-}p}$ and +20 $V_{p\text{-}p}$ at 80 kHz.

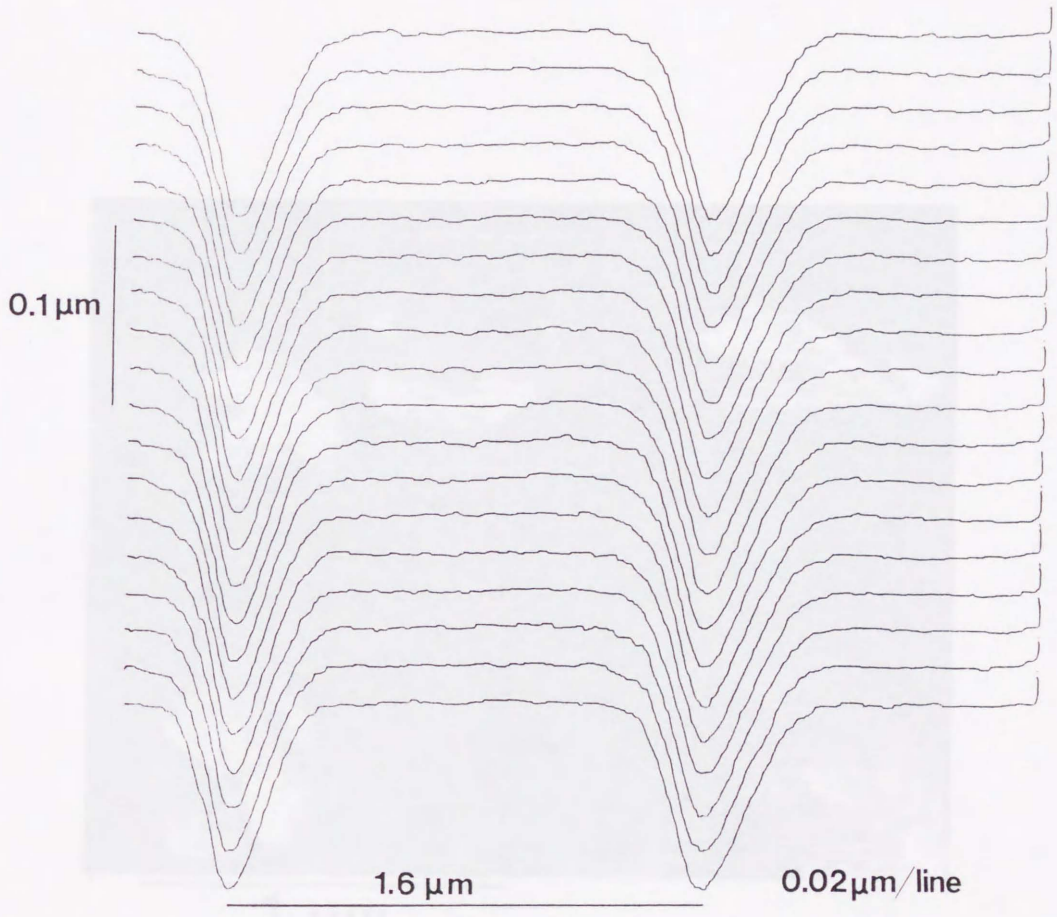

Fig. 4.3. Topography of an optical disk.

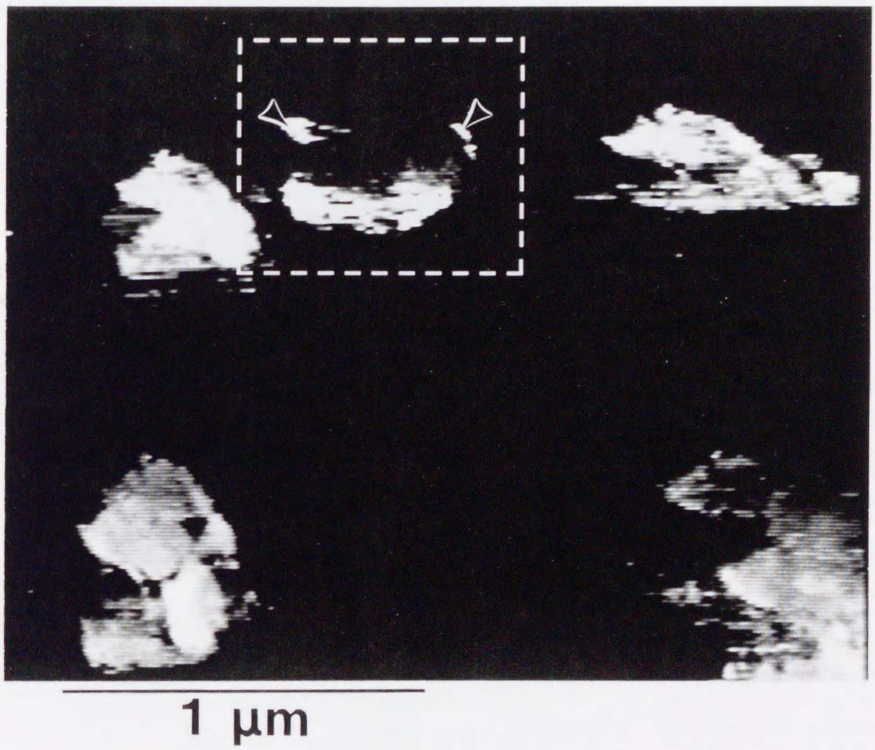

Fig. 4.4. Tunneling current image.

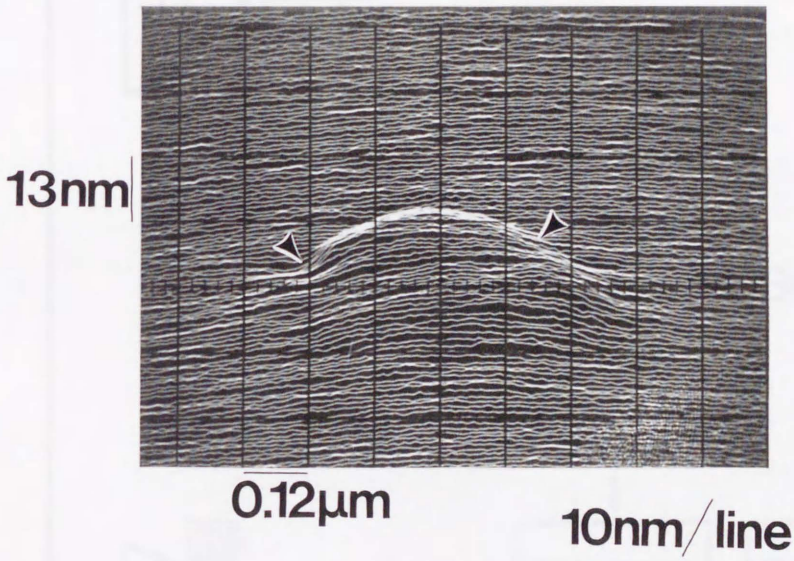

Fig. 4.5. Contour of a silicon surface.

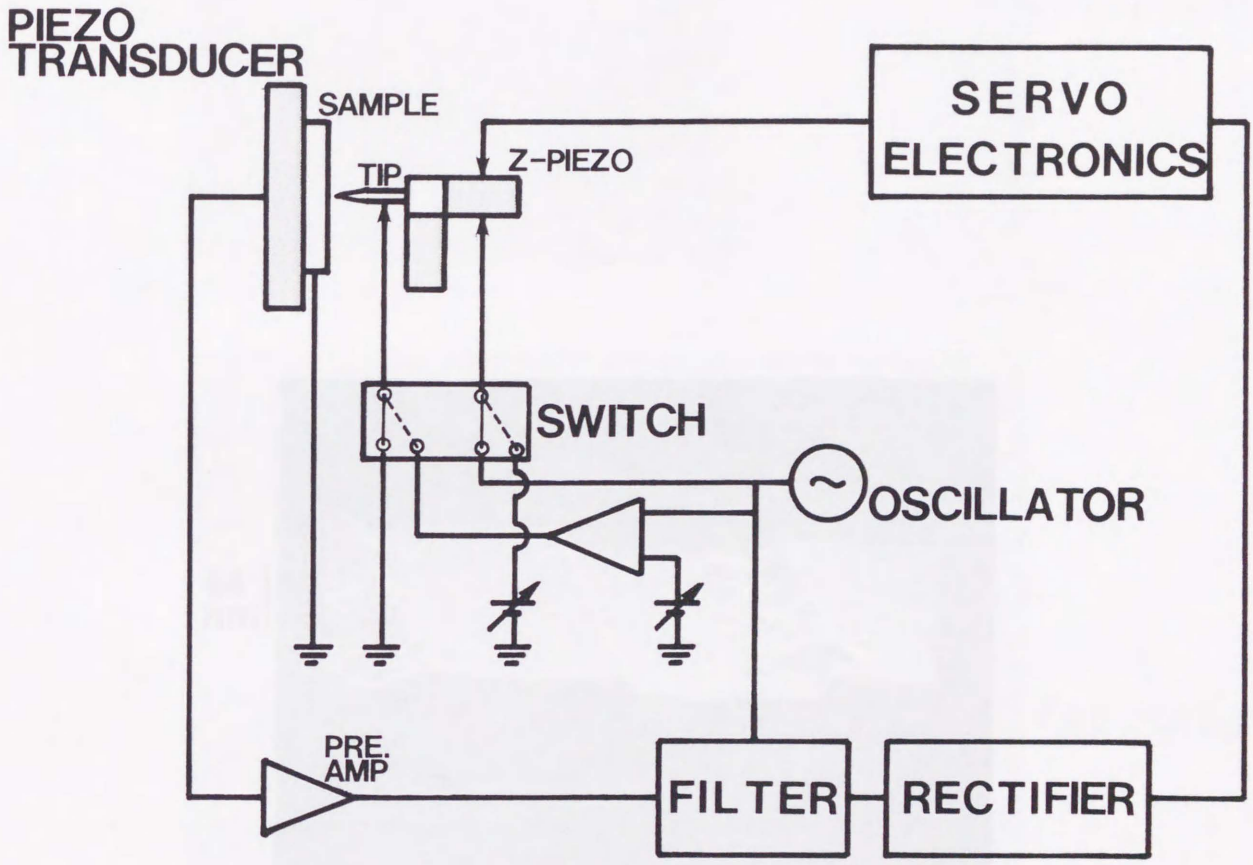

Fig. 4.6. Schematic diagram of electrostatic force imaging.

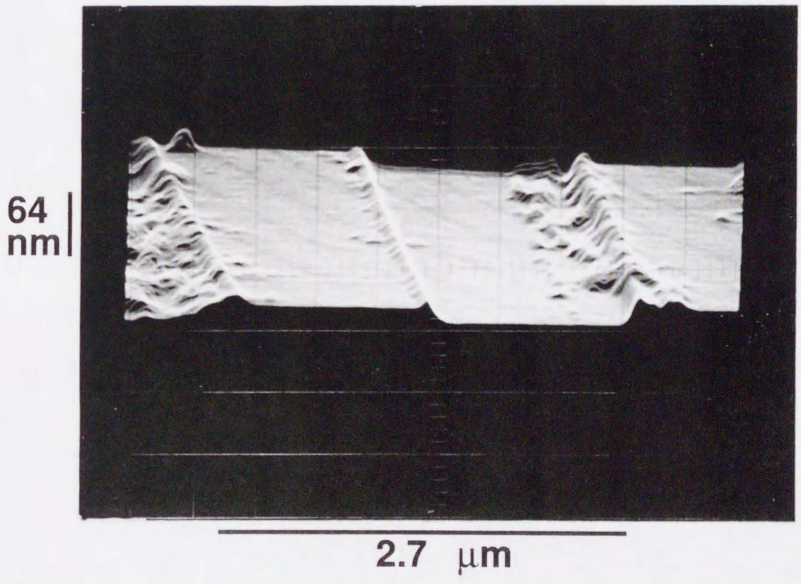

Fig. 4.7. Line profile image of topography.

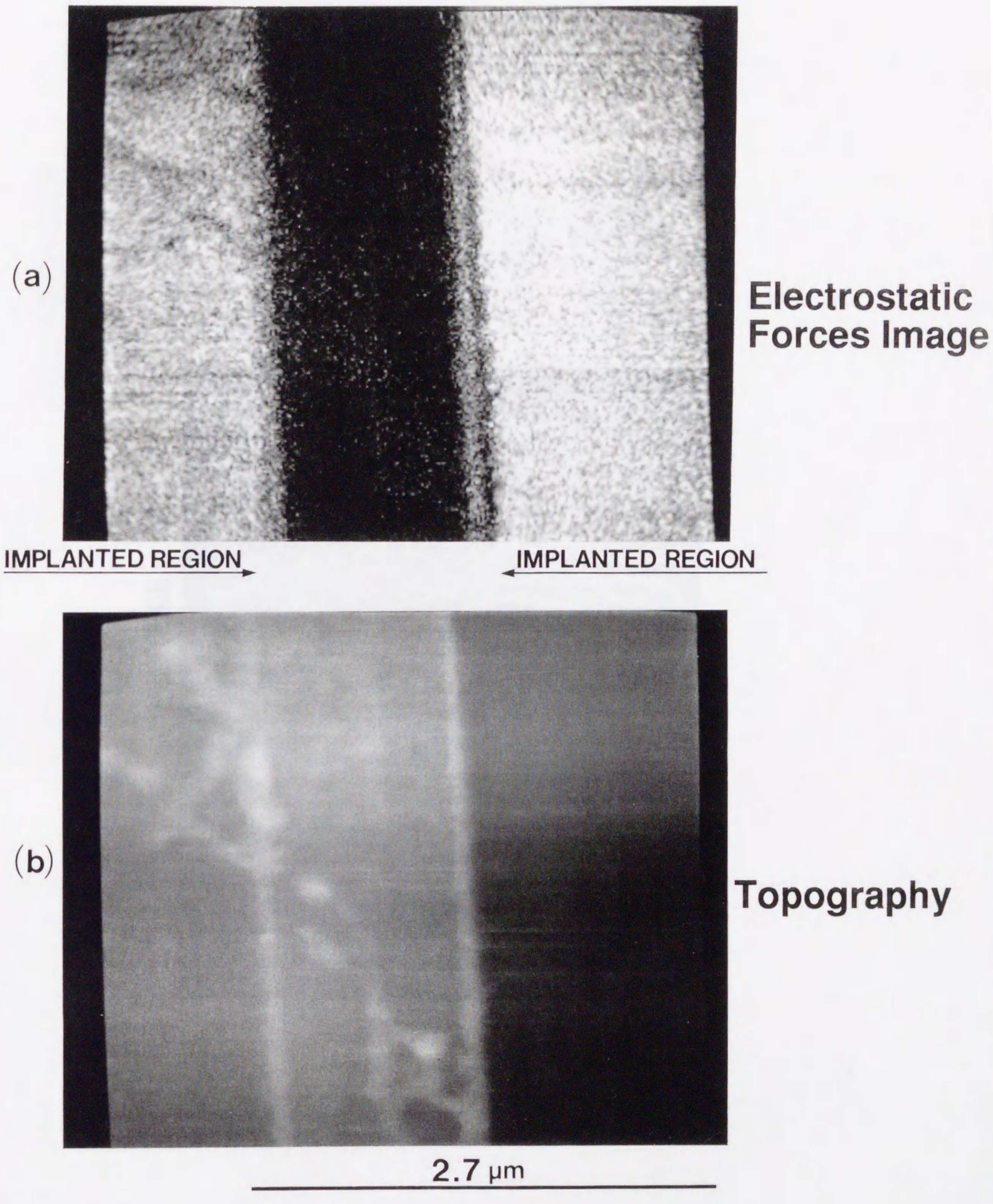

Fig. 4.8. Simultaneously taken electrostatic force image (a) and topography (b).

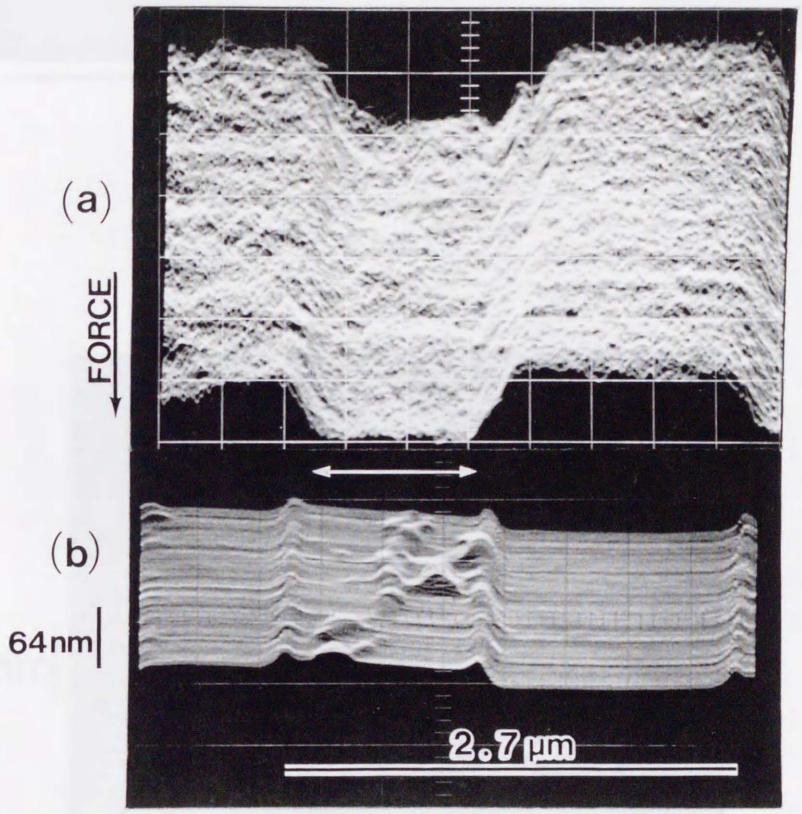

Fig. 4.9. Line profile images of electrostatic force (a) and topography (b).

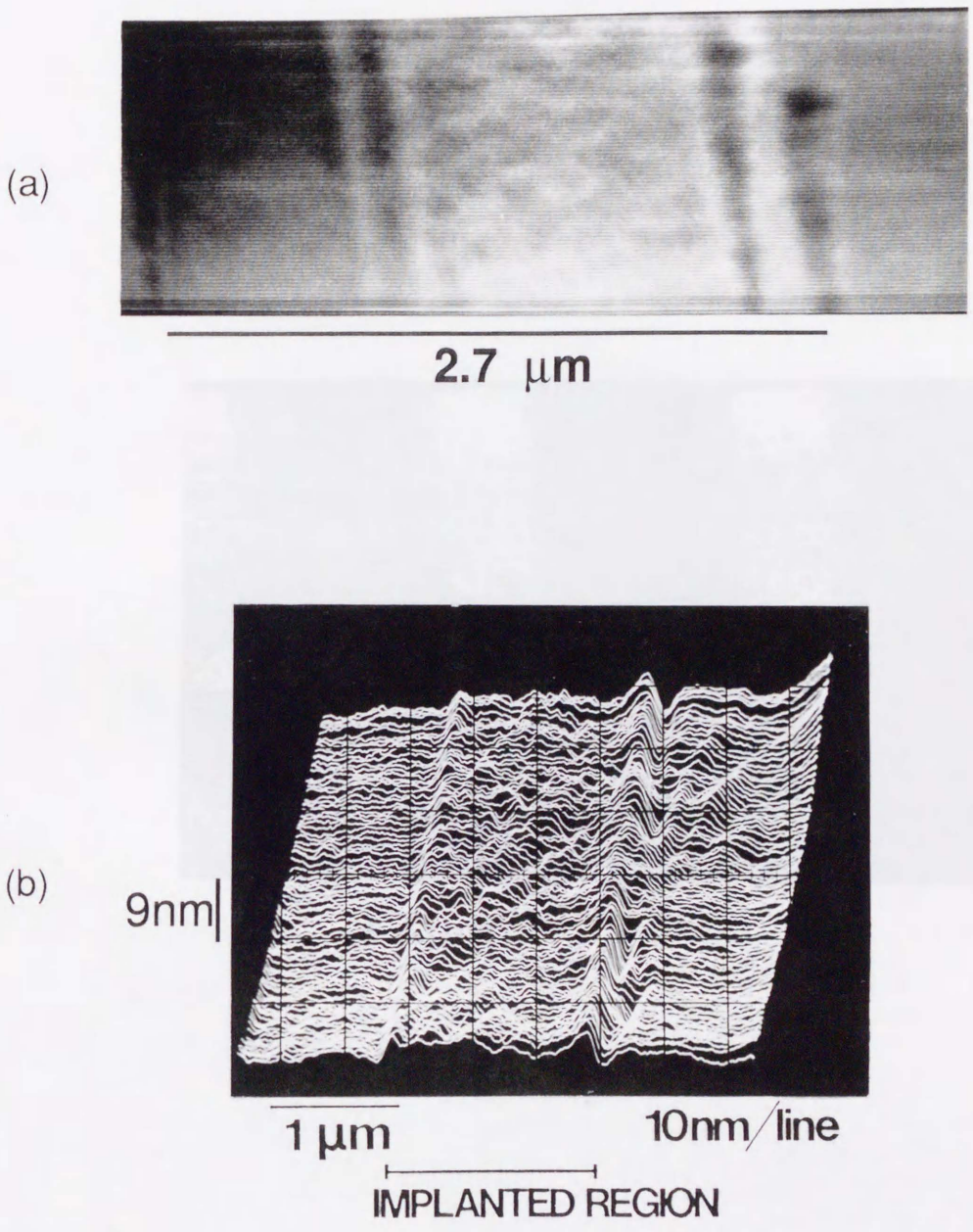

Fig. 4.10. Pre-annealing topography after etching:
(a) gray scale image, (b) line profile image.

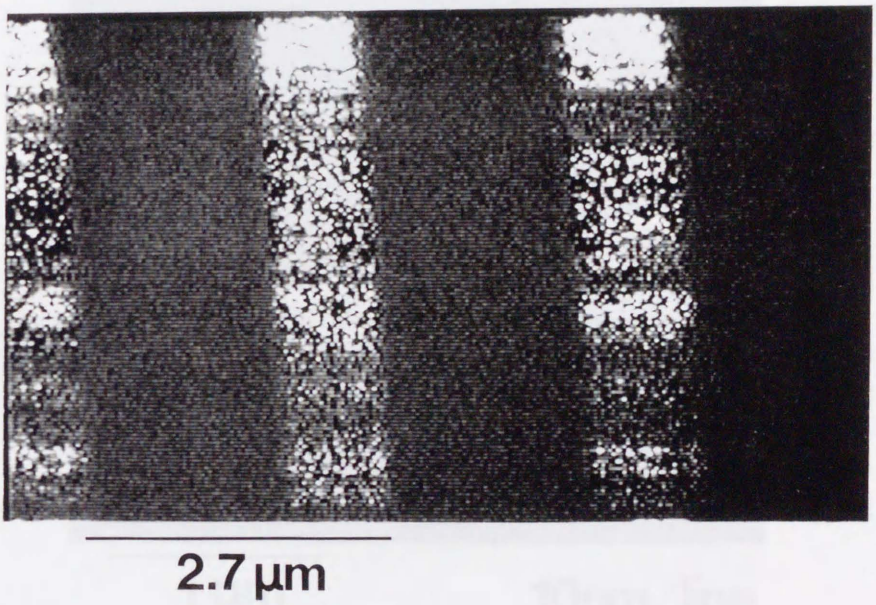

Fig. 4.11. Tunneling current image taken at a tip voltage of +6.9 V.

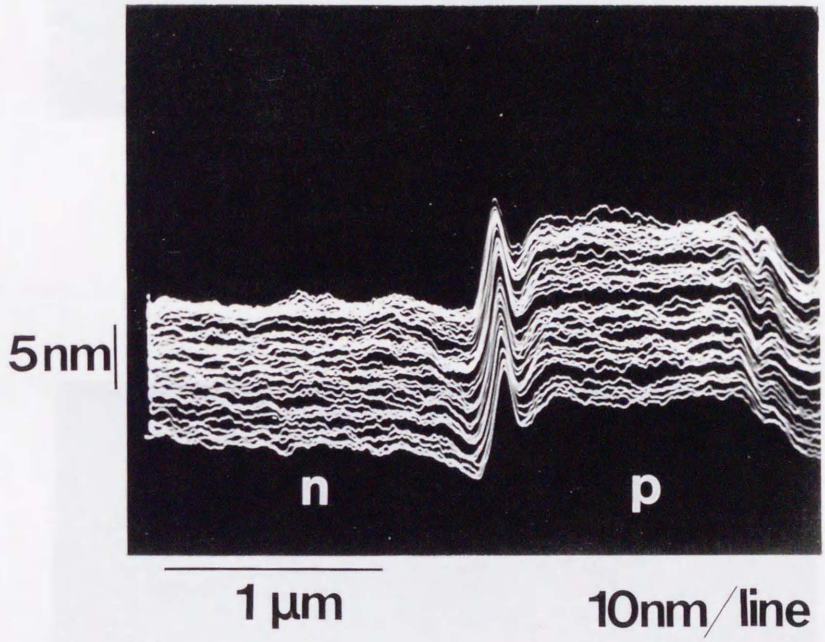

Fig. 4.12. After-annealing topography.

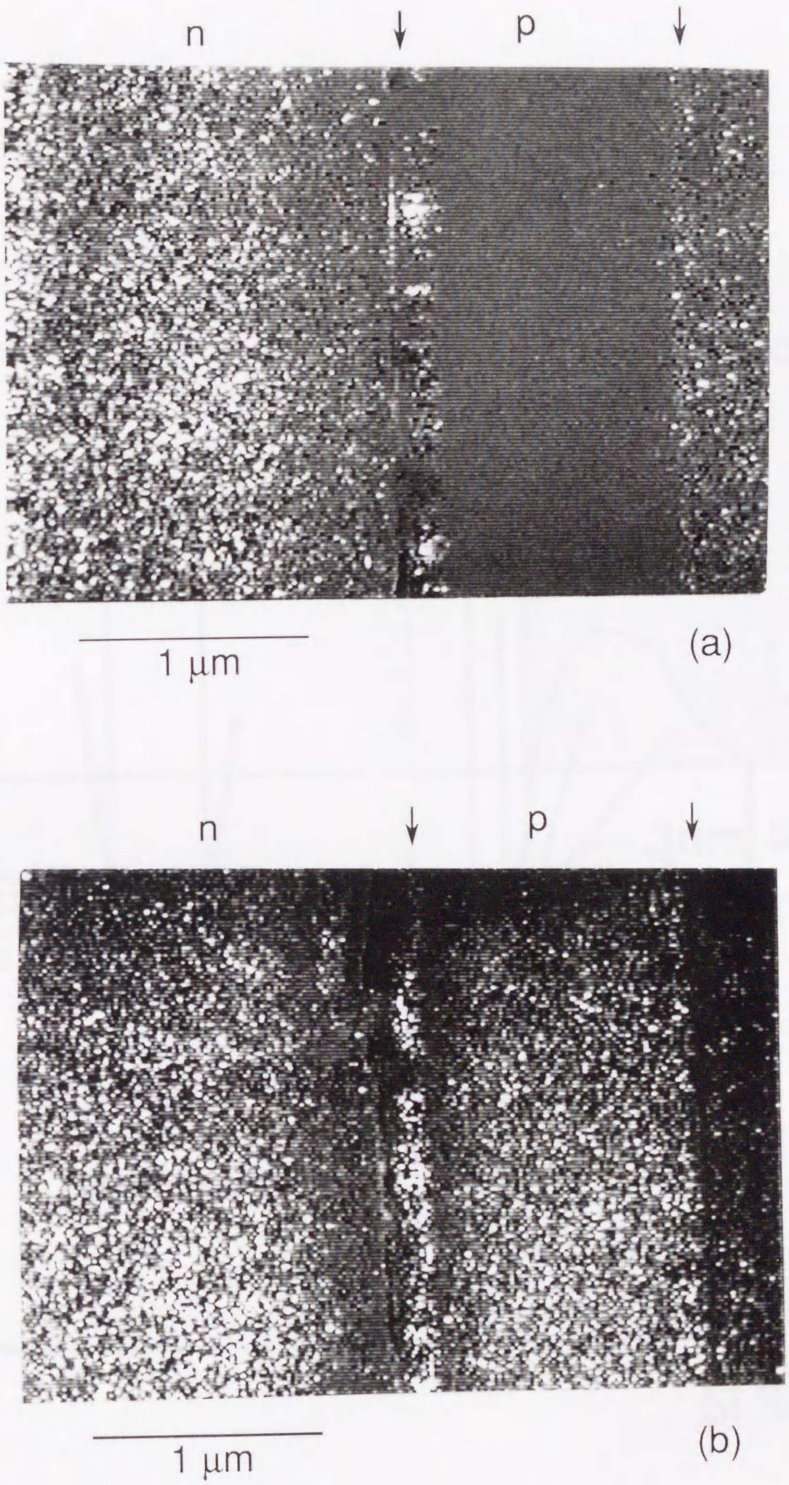

Fig. 4.13. Tunneling current images with (a) -1.9 V and (b) +1.9 V applied to tip.

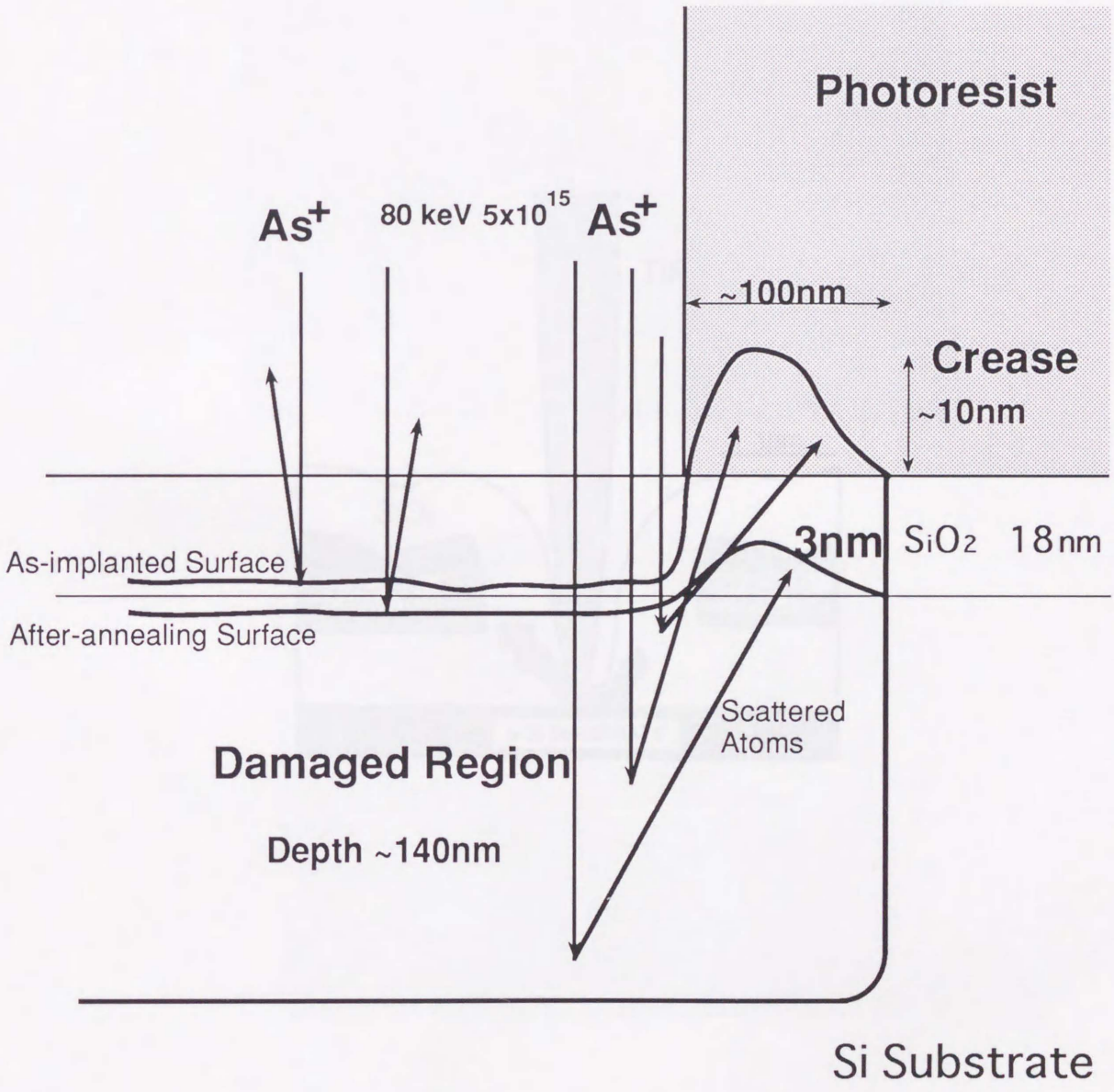

Fig. 4.14. Schematic cross section in the ion-implanted process.

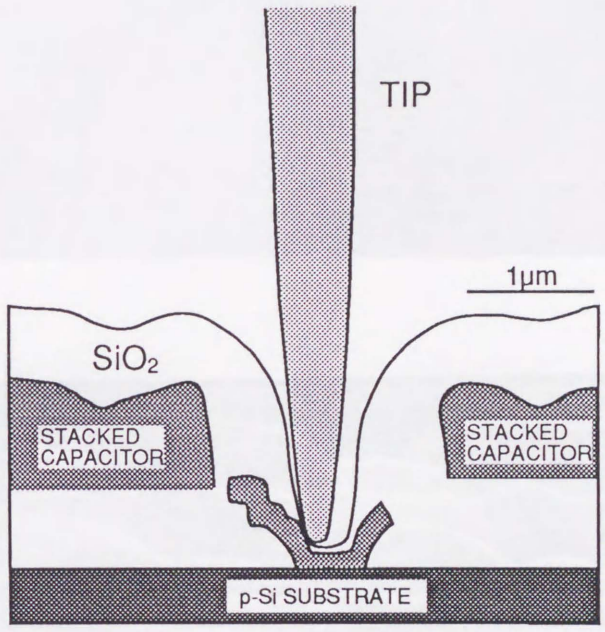

Fig. 4.15. Schematic cross-sectional structure of the sample and tip used in this observation.

(a)

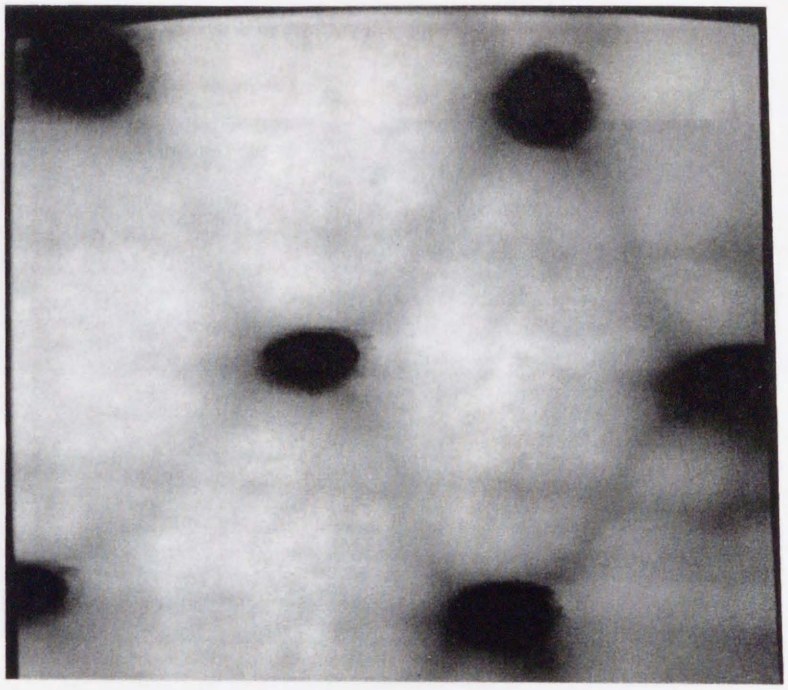

(b)

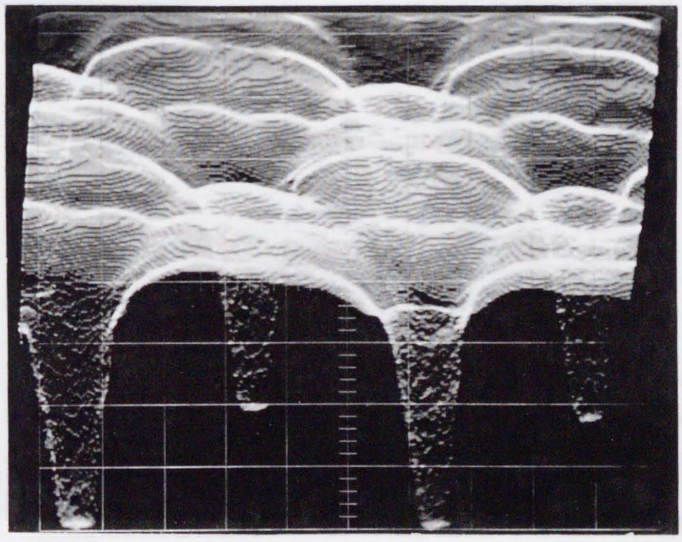

Fig. 4.16. Topography: (a) gray scale, (b) line profile. Scan area is 3 × 3 μm.

(a)

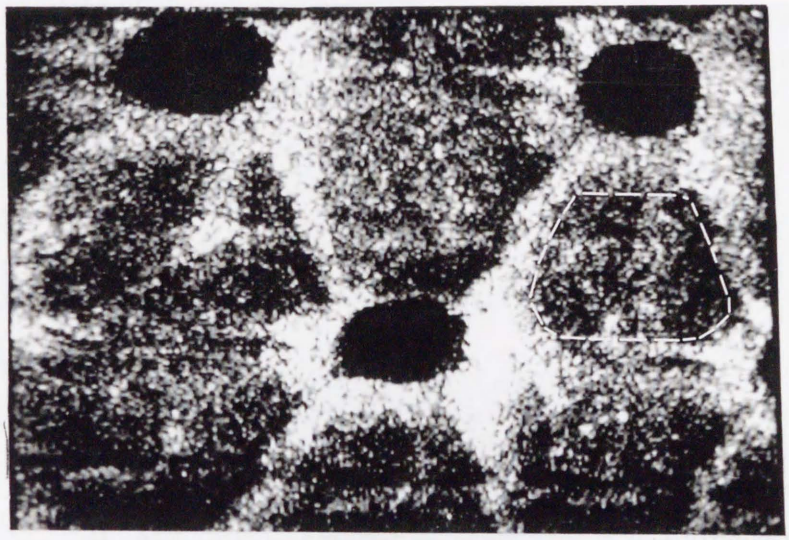

(b)

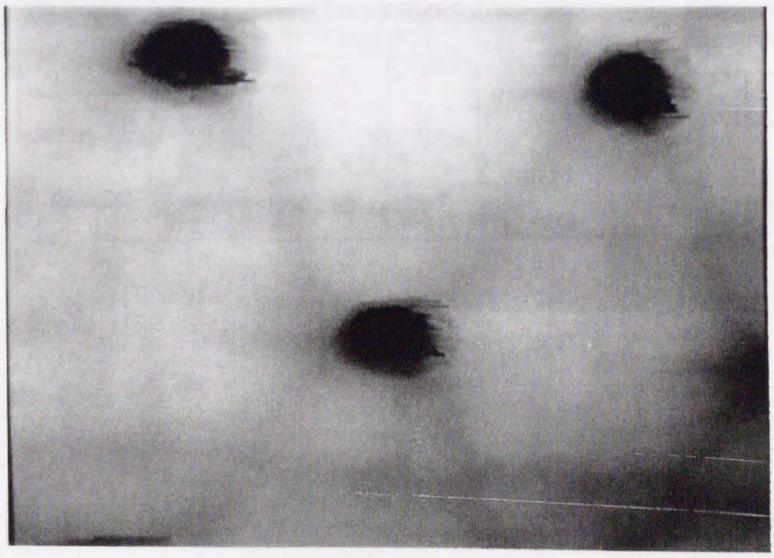

Fig. 4.17. Electrostatic force image (a) and topography (b) measured simultaneously. Dashed line indicates a buried stacked capacitor.

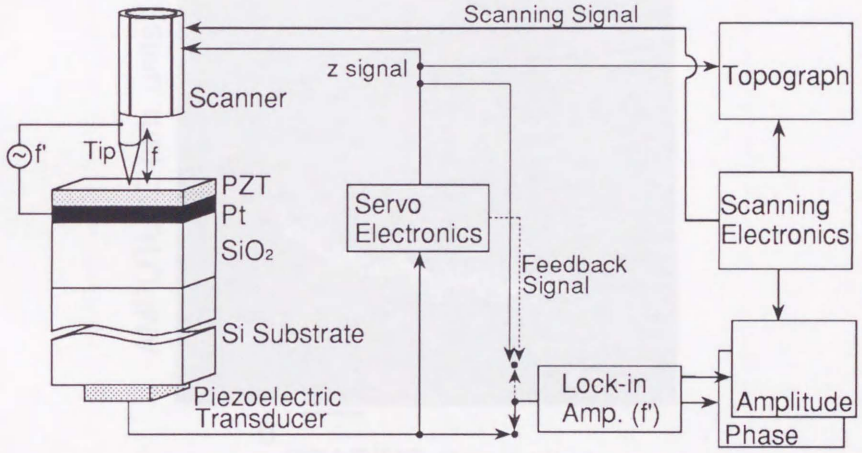

Fig. 4.18. Schematic diagram of strain imaging.

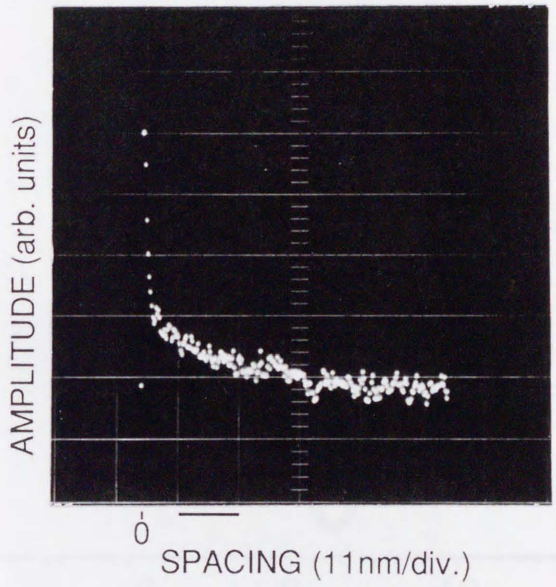

Fig. 4.19. Amplitude of generated vibration as a function of tip-to-sample spacing.

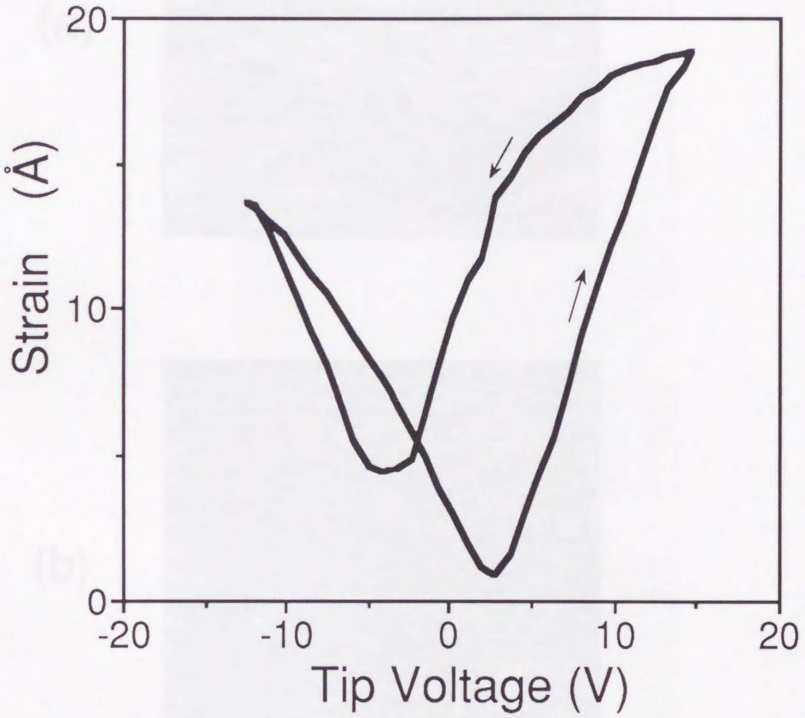

Fig. 4.20. Strains measured by surface-displacement detection as a function of tip voltage.

(a)

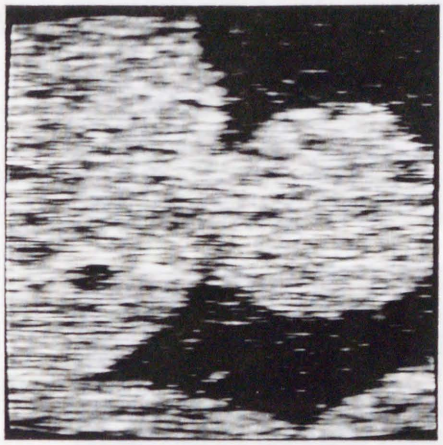

(b)

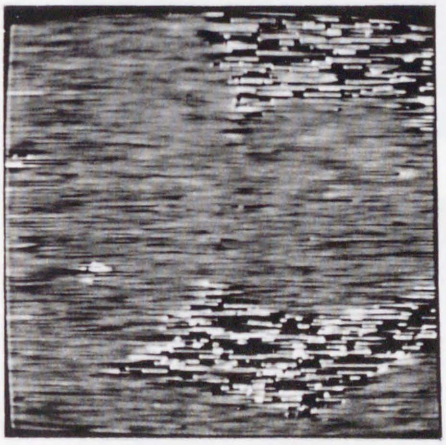

Fig. 4.21. Amplitude (a) and phase (b) of strain imaging obtained by surface-displacement detection.

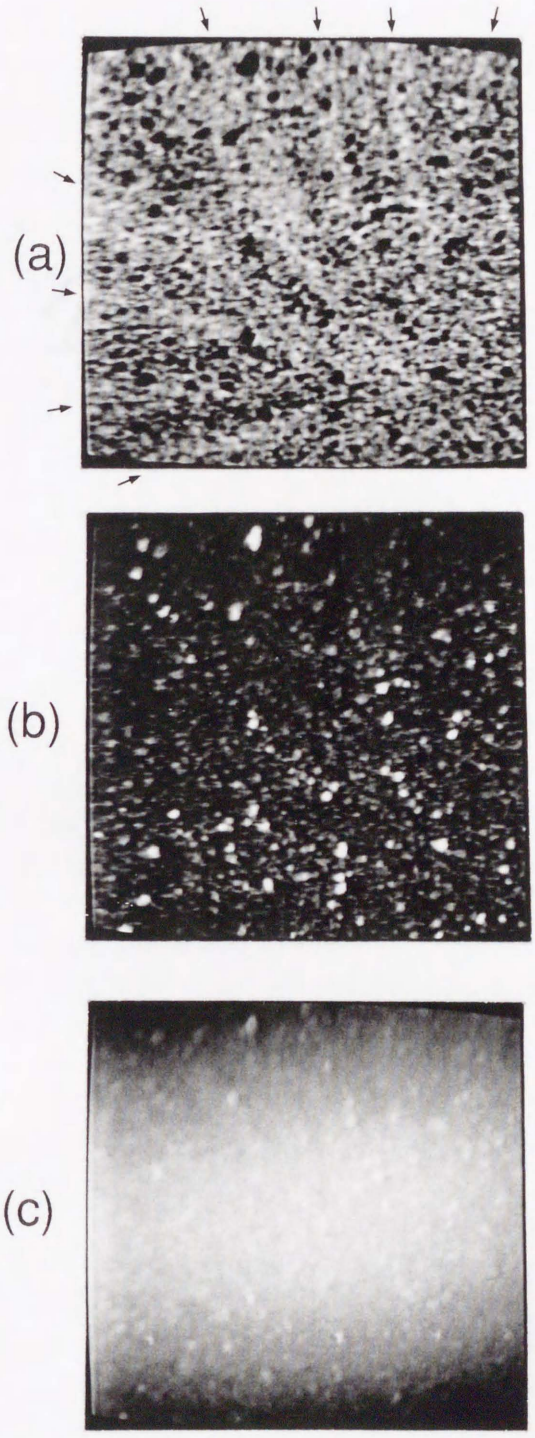

Fig. 4.22. Amplitude (a), phase (b), and topograph (c) of strain imaging obtained by vibration detection.

公 表 論 文

[1] Tunneling acoustic microscope

K. Takata, T. Hasegawa, S. Hosaka, S. Hosoki, and T. Komoda
Applied Physics Letters, Vol. **55**, No. 17 (1989) pp. 1718-1720.

[2] Tunneling Acoustic Microscope

K. Takata, J. Yugami, T. Hasegawa, S. Hosaka, S. Hosoki, and T. Komoda
Japanese Journal of Applied Physics, Vol. 28, No. 12 (1989) pp. L2279-L2280.

[3] Electrostatic Force Imaging by Tunneling Acoustic Microscopy

K. Takata, T. Okawa, and M. Horiuchi
Japanese Journal of Applied Physics, Vol. 30, No. 2B (1991) pp. L309-L312.

[4] Observation of deep contact holes and conductive components underlying insulator in a memory cell by tunneling acoustic microscopy

K. Takata, T. Kure, and T. Okawa
Applied Physics Letters, Vol. 60, No. 4 (1992) pp. 515-517.

[5] Strain Imaging of Lead-Zirconate-Titanate Thin Film by Tunneling Acoustic Microscopy

K. Takata, K. Kushida, K. Torii, and H. Miki
Japanese Journal of Applied Physics, Vol. 33, No. 5B (1994) pp. 3193-3196.

参考論文

[1] Scanning tunneling microscope with reliable coarse positioners

K. Takata, S. Hosoki, S. Hosaka, and T. Tajima
Review of Scientific Instruments, Vol. 60, No. 4 (1989) pp. 789-791.

[2] Tunneling Acoustic Microscopy (invited paper)

K. Takata
Proceedings of 12th Symposium on Ultrasonic Electronics, Tokyo 1991,
Japanese Journal of Applied Physics, Vol. 31 (1992) Supplement 31-1, pp. 3-8.

[3] Tunneling acoustic microscopy (invited paper)

K. Takata
Proceedings of 1992 IEEE Ultrasonics Symposium, Tucson
(IEEE, New York, 1992) pp. 723-729.